



Condensation flow patterns and heat transfer in horizontal microchannels



Ali H. Al-Zaidi^{a,b}, Mohamed M. Mahmoud^{a,c}, Tassos G. Karayiannis^{a,*}

^a College of Engineering, Design and Physical Sciences, Brunel University London, Uxbridge UB8 3PH, UK

^b University of Misan, Amarah 62001, Iraq

^c Faculty of Engineering, Zagazig University, Zagazig 44519, Egypt

ARTICLE INFO

Keywords:

Condensation
Heat transfer
Flow patterns
Microchannel
Correlations

ABSTRACT

An experimental investigation was carried out to study the effect of refrigerant mass flux, local vapour quality, coolant flow rate and inlet coolant temperature on the local condensation heat transfer coefficient. Flow visualization was also conducted to capture flow patterns during flow condensation using a high-speed camera integrated with a microscope. HFE-7100, a dielectric and eco-friendly refrigerant was used in rectangular multi-microchannels with a hydraulic diameter of 0.57 mm. Experiments were performed at a saturation temperature of 60 °C, mass flux range 48–126 kg/(m² s), coolant flow rate range 0.5–1.1 L/min and inlet coolant temperature range 20–40 °C. The results showed that the local condensation heat transfer coefficient increases with increasing mass flux and decreases with decreasing local vapour quality. A negligible effect of the coolant side conditions, saturation-to-wall temperature difference, on the local condensation heat transfer coefficient was found. The main flow regime was annular flow, while slug and bubbly flow were found at some operating conditions. The experimental results were compared with the existing correlations for heat transfer rates. Also, two existing flow pattern maps, for conventional and mini/microchannels, were used to compare the current flow pattern results.

1. Introduction

The dissipation of high heat fluxes from small areas with uniform surface temperature is one of the greatest challenges in the thermal design of semiconductor electronic devices. Two phase flow boiling in microchannels is one of the promising cooling techniques that can dissipate high heat fluxes at nearly uniform surface temperature (slightly higher than the saturation temperature). This is due to a number of advantages: high heat transfer rate, small size, light weight and small fluid charge (small amount enters the atmosphere if leakage occurs). Accordingly, a large number of researchers such as [1–3] focused on studying flow boiling characteristics in microchannels. This was motivated by the lack of understanding several fundamental issues in flow boiling such as the dominant heat transfer mechanism(s), flow instability, boiling incipience, mechanisms of dryout and the prediction of heat transfer rates and pressure drop. With the assumption that these fundamental issues are resolved and the possibility of designing and fabricating multi-microchannel evaporators, the design of a small scale pumped loop cooling system is then the next challenge. This difficulty arises from the basic fundamental knowledge in designing appropriate small/micro condensers, whose size might be significant depending on the final heat sink (ambient air or water for example) compared to the

size of a small scale pumped loop cooling system. There are very limited numbers of studies in the literature focused on studying condensation in multi-microchannel configurations. Therefore, the objective of the present study is to investigate experimentally the thermal performance of a multi-microchannel condenser. It is commonly agreed that flow boiling characteristics in microchannels are different compared to conventional large diameter channels. Similarly, condensation in microchannels may also differ compared to large diameter channels. For example, the dominant forces that might affect the condensation mechanism in microchannels may be different compared to that in larger channels. Del Col et al. [4] reported that the condensation mechanism depends on the relative importance of the surface tension, gravity and shear forces, which, in turn, depend on several parameters, such as vapour quality, mass flux, fluid properties and channel geometry. In larger tubes, the gravity and shear forces are more dominant, while in mini/microchannels, the surface tension force can also become important. Del Col et al. [5] mentioned that in non-circular mini/microchannels, the surface tension force can pull the liquid phase towards the channel corners leading to a thin liquid film and low thermal resistance at the flat sides. This means that the heat transfer coefficient in non-circular channels is expected to be higher compared to circular channels. Kim and Mudawar [6] reported that, when the mass flux increases,

* Corresponding author at: College of Engineering, Design and Physical Sciences, Brunel University London, Uxbridge, Middlesex UB8 3PH, UK.
E-mail addresses: mbasuny@zu.edu.eg (M.M. Mahmoud), tassos.karayiannis@brunel.ac.uk (T.G. Karayiannis).

Nomenclature

<i>A</i>	area [m ²]
<i>b</i>	length of channel side [m]
<i>Bo</i>	bond number [-] $Bo = (\rho_l - \rho_g) * g * D_h^2 * \sigma^{-1}$
<i>Bo_{cr}</i>	critical Bond number [-] $Bo_{cr} = 1 / [\rho_l * (\rho_l - \rho_g)^{-1} - \pi / 4]$
<i>C_p</i>	specific heat at constant pressure [J/kg K]
<i>D_h</i>	hydraulic diameter [m]
<i>f</i>	fanning friction factor [-]
<i>G</i>	mass flux [kg/m ² s]
<i>g</i>	gravitational acceleration [m/s ²]
<i>H</i>	height [m]
<i>h, HTC</i>	heat transfer coefficient [W/m ² K]
<i>h_{LT}</i>	heat transfer coefficient with total mass flowing as liquid [W/m ² K]
<i>h_{NU}</i>	heat transfer coefficient, the Nusselt equation [W/m ² K]
\bar{h}	average heat transfer coefficient [W/m ² K]
<i>i_g</i>	latent heat of vaporization [J/kg]
<i>J_G</i>	dimensionless vapour velocity [-] $J_G = G * x / (g * D_h * \rho_g * \Delta\rho)^{0.5}$
<i>k</i>	thermal conductivity [W/m K]
<i>K₉₀</i>	loss coefficient for the 90° turns [-]
<i>L</i>	length [m]
<i>m</i>	fin parameter, $\sqrt{2h/k_{cu} * W_{fin}}$
\dot{m}	mass flow rate [kg/s]
<i>MAE</i>	mean absolute error
<i>N</i>	number of channels [-]
\overline{Nu}	average Nusselt number [-] $\overline{Nu} = \bar{h} * D_h * k_f^{-1}$
<i>P</i>	pressure [Pa]
<i>Pr</i>	Prandtl number [-] $Pr = c_{p_l} * \mu_l * k_f^{-1}$
<i>P_R</i>	reduced pressure [-] $P_R = P_i / P_{cr}$
<i>Q</i>	heat rate [W]
q''	heat flux [W/m ²]
\bar{q}''	average heat flux [W/m ²]
<i>Re</i>	Reynolds number [-] $Re = G * D_h * \mu_l^{-1}$
<i>Re_{ls}</i>	superficial liquid Reynolds number [-] $Re_{ls} = G(1-x) * D_h * \mu_l^{-1}$
<i>Re_{gs}</i>	superficial vapour Reynolds number [-] $Re_{gs} = G * x * D_h * \mu_g^{-1}$
<i>Su_{go}</i>	vapour only Suratman number [-] $Su_{go} = \rho_g * \sigma * D_h * \mu_g^{-2}$
<i>T</i>	temperature [K]
<i>v</i>	specific volume [m ³ /kg]
<i>W</i>	width [m]
<i>W_c</i>	centre to centre distance of microchannel widths [m]
<i>We</i>	Weber number [-] $We = G^2 * D_h * (\rho * \sigma)^{-1}$
<i>We*</i>	modified Weber number [-] $We^* = 2.45(Re_{gs}^{0.64} / Su_{go}^{0.3} (1 + 1.09X_{tt}^{0.039})^{0.4})$
<i>x</i>	vapour quality [-]
<i>X</i>	Lockhart–Martinelli parameter [-] $X = [(dP/dz)_l / (dP/dz)_g]^{0.5}$
<i>y1</i>	vertical distance between thermocouple and channel bottom [m]
<i>y2</i>	vertical distance between thermocouples [m]
<i>Z</i>	Shah's correlating parameter [-] $Z = (1/x-1)^{0.8} * P_R^{0.4}$

z axial distance [m]**Greek symbols**

α	area ratio [-] $\alpha = A_{sec,min} / A_{sec,max}$
β	aspect ratio [-] $\beta = W_{ch} / H_{ch}$
ΔP	pressure drop [Pa]
η	fin efficiency [-]
Θ	percentage predicted within $\pm 30\%$ of data
μ	viscosity [Pa s]
ρ	density [kg/m ³]
σ	surface tension [N/m]
\emptyset	two-phase pressure drop multiplier [-]

Subscripts

<i>3</i>	based on three-sided heat transfer in rectangular channel
<i>4</i>	based on four-sided heat transfer in rectangular channel
<i>b</i>	base
<i>B</i>	bottom
<i>ch</i>	channel
<i>cr</i>	critical
<i>cu</i>	copper
<i>eq</i>	equivalent
<i>exp</i>	experiment
<i>f</i>	fluid
<i>fin</i>	channel fin
<i>fi</i>	fluid in
<i>fo</i>	fluid out
<i>g</i>	gas or vapour
<i>ht</i>	heat transfer
<i>i</i>	inlet
<i>ip</i>	inlet plenum
<i>l</i>	liquid
<i>meas</i>	measured
<i>o</i>	outlet
<i>op</i>	outlet plenum
<i>p</i>	plenum
<i>pred</i>	predicted
<i>sat</i>	saturation
<i>sc</i>	sudden contraction
<i>se</i>	sudden expansion
<i>sec</i>	section
<i>sp</i>	single phase
<i>T</i>	top
<i>tp</i>	two phase
<i>tt</i>	turbulent liquid-turbulent vapour
<i>wi</i>	internal wall surface
<i>wti</i>	water in
<i>wto</i>	water out
<i>z</i>	axial local

interfacial shear stress increases. This leads to a thinner liquid film and higher heat transfer coefficient. As mentioned above, in larger tubes, gravity force could also affect the heat transfer coefficient by draining the liquid condensed to the channel bottom leading to a thicker liquid film. Moreover, Zhang and Li [7] studied numerically the effect of gravity force ($g = 0 \text{ m/s}^2$, $g = 9.81 \text{ m/s}^2$ and $g = 19.6 \text{ m/s}^2$) on flow condensation in horizontal single tubes with diameter 0.25–4 mm. They reported that when the gravity force increases, the liquid film becomes thinner at the upper section of the tube leading to low thermal resistance and thus high transfer coefficient. Their simulation results

indicated that nearly two-thirds of the tube perimeter was lubricated with a thin liquid film (small thermal resistance and thus high heat transfer coefficient). In other words, the contribution of the upper section of the tube to the heat transfer rate is more pronounced compared to the lower section of the tube. In the following sub-sections, the flow patterns, heat transfer coefficient, pressure drop and heat transfer correlations are reviewed and discussed.

1.1. Flow patterns

Various flow patterns were observed during flow condensation in several experimental and numerical studies. Some researchers studied flow condensation in multi-microchannel configurations. For example, Ma et al. [8] studied flow condensation of steam in trapezoidal silicon multi-microchannels with a hydraulic diameter of 0.134, 0.138 and 0.165 mm. Their experiments were conducted at a mass flux range of 90–290 kg/m² s. They captured four flow patterns namely: annular, droplet, injection and bubble flow. No slug flow was observed. The annular flow was described as a vapour core surrounded by a liquid film. It was reported that the condensate film thickness on the side walls in annular flow varies with time for the same location and operating conditions. These variations in liquid film thickness were attributed to two reasons: (1) the interfacial instability arising from the velocity difference between liquid and vapour and (2) the merging of the condensate into the liquid film during the condensation process. The droplet flow was characterized by small droplets growing in size on the bottom wall of the channel while the condensate liquid film covered the side walls. The growth of the droplets was due to condensation and merging with other small droplets. The injection flow was found as a transition regime between annular flow and bubble flow. In this regime, the condensate film thickness on the side walls increases along the axial direction. When the condensate thickness becomes large enough, the liquid slug forms and vapour bubbles are released leading to the formation of bubbly flow. The axial location at which the injection flow (formation of bubbly flow) occurs was found to move towards the channel exit as the mass flux and inlet vapour quality increases, i.e. the high flow inertia induced by high mass flux promotes the core of vapour to travel a long distance along the channel. Also, they reported that the annular/droplet flow expanded and spanned along the channels when the mass flux and vapour quality increased. Chen et al. [9] investigated the condensation of steam in triangular silicon multi-microchannels with a hydraulic diameter of 0.25 and 0.1 mm. Droplet, annular, injection and slug-bubbly flow were observed. They reported that, when the mass flux or the hydraulic diameter increased at the same Reynolds number, the injection location moved towards the channel outlet. In contrast, different flow patterns were found by Kim et al. [10] who investigated the flow condensation of FC-72 in a copper multi-microchannels condenser of square cross sectional area and 1 mm hydraulic diameter and length of 299 mm. The experiments were conducted at mass flux ranging from 68 to 367 kg/m² s, coolant mass flow rate of $3\text{--}6 \times 10^{-3}$ kg/s and saturation temperature of 57.2 and 62.3 °C. A high-speed camera was used to capture the flow patterns during the experiments. They reported that smooth-annular, wavy-annular, transition, slug and bubbly flow were observed. The transition regime was identified as bridging of liquid ligaments through the vapour core. They found that, when the mass flux increased, the smooth-annular flow extended towards the low quality region, while the slug flow became narrow in this region. Jiang et al. [11] conducted a visualization investigation of ethanol–water in trapezoidal silicon multi-microchannels with a hydraulic diameter of 0.165 mm and channel length of 50 mm. Six inlet ethanol concentrations of 2%, 4%, 6%, 20%, 31% and 60% were tested. A camera system integrated with a set of microscope lenses was used to capture the flow patterns during their experiments. They reported that annular, annular-streak, annular-streak-droplet, churn, injection, droplet-injection and bubble flow were observed. The annular-streak flow was characterized by a thick streak that generated from the bottom liquid film of the channel, while some droplets were observed in the annular-streak-droplet regime. The injection flow was found in all experiments. They reported that, there were two dominant types of this regime, namely droplets-injection and injection flow. Comparing these results to pure steam condensation flow patterns observed in Ma et al. [8], who used the same test section and experimental system, indicates significant effects for ethanol on flow patterns. They concluded that as ethanol concentration increases (the surface free

energy difference increases), the condensation mechanism changes from a filmwise condensation to a transition state followed by dropwise condensation mechanism.

Some other researchers studied flow condensation in single channels. For instance, Chen et al. [12] conducted a numerical study of the flow condensation of FC-72 in a rectangular microchannel with a hydraulic diameter of 1 mm using the Volume of Fluid method (VOF). In their simulation and at mass flux of 100–150 kg/m² s, five flow patterns were reported, namely; smooth-annular, wavy-annular, transition, slug and bubbly flow, as in [10] above. They reported that, when the cooling heat rate decreased or mass flux increased, the vapour column length increased along the channel, and the initial bubble size increased. El Achkar et al. [13] carried out an experimental study of flow condensation of n-pentane in a transparent square microchannel with a hydraulic diameter of 0.553 mm. Their experiments were carried out at low mass fluxes ranging from 3.78 to 11.98 kg/m² s. They reported that annular, intermittent and spherical bubble flows were the main regimes. The intermittent flow was identified as a slug flow or elongated bubble flow.

It can be concluded, from the above studies, that the names and features of the condensation flow patterns differ from one study to another. This could be due to the fact that different fluids, operating conditions and channel geometries were examined. However, at this stage no final conclusion can be made on the most common or prevailing flow patterns.

1.2. Heat transfer

Several experimental and theoretical studies in both mini and microchannel condensers have been conducted to understand the effect of control parameters such as mass flux, vapour quality, saturation temperature, channel geometry and coolant side conditions on the condensation heat transfer coefficient. For example, Wang and Rose [14] and Zhang and Li [7] conducted a numerical study on flow condensation in non-circular and circular microchannels, respectively. Wang and Rose [14] indicated that, for part of the channel, the local averaged heat transfer coefficient (averaged along the perimeter) was independent of mass flux (shear stress), gravity and axial distance (local vapour quality). As the vapour mass flux increases (shear stress increases), the length of this part of channel along which the heat transfer coefficient remains almost constant also increases. They reported that, the surface tension was the dominant regime for this part. Zhang and Li [7] presented steady three dimensional simulations of R410A in horizontal mini/micro tubes with inner diameter ranging from 0.25 to 4 mm at a mass flux ranging from 400 to 1000 kg/m² s. The VOF method was adopted in this simulation to track the vapour-liquid interfaces. Their results showed that the local heat transfer coefficient increased with increasing mass flux. Also, they varied the gravity force from 0 to 19.62 m/s² to study the effect of this parameter on the heat transfer coefficient. They reported that in the 4 mm diameter tube and at low quality and mass flux, higher gravity force led to heat transfer enhancement by thinning liquid film at the upper wall. Moreover, they mentioned that, when gravity increased, the liquid film thickness at the bottom wall became thicker. However, this part had a smaller effect compared to the upper part on the heat transfer rates, according to Da Riva and Del Col [15].

Contrary to the above mentioned numerical studies, several researchers such as [16–18,21–23] investigated experimentally flow condensation in microchannels and agreed on the effect of mass flux and average vapour quality on the average heat transfer coefficient. The experimental conditions covered in these studies are summarized in Table 1. They concluded that the average heat transfer coefficient plotted versus average vapour quality increased with increasing mass flux. In these studies, the average heat transfer coefficient was calculated using the average heat flux (from an energy balance on the coolant side and the surface area), the average saturation temperature

Table 1
Summary of the numerical and experimental conditions covered in past flow condensation studies.

Author(s)	Channel geometry ^a	Channel material	D_h (mm)	Fluid(s)	T_{sat}/G
Cavallini et al. [16]	R, M	Aluminium	1.4	R134a, R410A	40 °C 200–1400 kg/m ² s
Agarwal et al. [17]	D, M	Aluminium	0.424–0.839	R134a	55 °C 150–750 kg/m ² s
Matkovic et al. [25]	Sq, S	Copper	1.18	R134a	40 °C 200–800 kg/m ² s
Wang and Rose [14]	R, T, S	–	0.5–2	R134a, R22, R410A, Ammonia, R152a, Propane, CO ₂	25 and 50 °C 100–1300 kg/m ² s
Fronk and Garimella [18]	C, S	Stainless steel	1.435	Ammonia	30–60 °C 75 and 150 kg/m ² s
Kim and Mudawar [6]	Sq, M	Copper	1	FC-72	57.2–62.3 °C 68–367 kg/m ² s
Al-Hajri et al. [21]	R, S	Copper	0.7	R134a, R245fa	30–70 °C 50–500 kg/m ² s
Heo et al. [22]	R, M	Aluminium	1.5	CO ₂	–5–5 °C 400–1000 kg/m ² s
Liu et al. [24]	Sq, C, S	Stainless steel	0.952 and 1.152	R152a	40 and 50 °C 200–800 kg/m ² s
Bortolin et al. [26]	Sq, C, S	–	1	R134a	40 °C 400 and 800 kg/m ² s
Sakamatapan and Wongwises [31]	R, M	Aluminium	1.1 and 1.2	R134a	35–45 °C 345–685 kg/m ² s
Goss et al. [32]	C, M	Copper	0.77	R134a	28–38 °C 230–445 kg/m ² s
Illán-Gómez et al. [23]	R, M	Aluminium	1.16	R1234yf, R134a	30–55 °C 350–940 kg/m ² s
Zhang and Li [7]	C	–	0.25–4	R410 A	46.85 °C 400–1000 kg/m ² s

^a S: single channel, M: multi-channel, Sq: square, R: rectangular, C: circular, T: triangular, D: different shapes (e.g. rectangular, square, triangular, barrel, N and W-shaped).

along the condenser and the averaged surface temperature. The average vapour quality was the average of the inlet and outlet vapour quality. In some studies, Fronk and Garimella [18], the heat transfer coefficient was calculated using the Log Mean Temperature Difference approach. The increase in the heat transfer coefficient with mass flux and vapour quality was attributed by Fronk and Garimella [18] to the thinning of the liquid film as the mass flux and vapour quality increases. Del Col et al. [19] investigated condensation heat transfer characteristics of R1234ze(E) in a horizontal rectangular channel having hydraulic diameter of 0.96 mm in the mass flux range 100–800 kg/m² s. For mass flux values equal to or > 200 kg/m² s, it was found that the heat transfer coefficient increases rapidly with mass flux and vapour quality, while for mass fluxes below 200 kg/m² s the heat transfer coefficient increased slightly with vapour quality. The same conclusion was reported by Jige et al. [20]. They investigated condensation heat transfer characteristics of four refrigerants; R134a, R32, R1234ze(E) and R410A in a horizontal multi-port tube of rectangular cross section and 0.85 mm hydraulic diameter. The mass flux ranged from 100 to 500 kg/m² s. For mass flux values above 100 kg/m² s, the results indicated that the heat transfer coefficient decreases monotonically as the vapour quality decreases which was attributed to the decrease in shear stress and the increase in condensate thermal resistance. In contrast, for the lowest mass flux (100 kg/m² s), the heat transfer coefficient exhibited a plateau in the vapour quality range 0.2–0.6, i.e. it did not decrease continuously as was the case for high mass fluxes. The trend at the lowest mass flux in the vapour quality range 0.2–0.6 was attributed to the dominance of surface tension force over vapour shear stress and gravity forces. Additionally, the values of the condensation heat transfer coefficient for R32 were 1.2–1.5 times greater than those measured for R134a and R1234ze(E) which was attributed to the higher liquid thermal conductivity (1.5–1.6 times higher) compared to R134a and

R1234ze(E).

Some researchers such as [18,21–24] investigated the effect of saturation temperature on the condensation heat transfer coefficient, see Table 1. They agreed on that the heat transfer coefficient increases as the saturation temperature decreases. The fact that the heat transfer coefficient decreases when increasing the saturation temperature was attributed by Fronk and Garimella [18] to the reduction in the density ratio and interfacial shear stress, and by Al Hajri et al. [21] to an increase in the vapour density that led to decreased vapour velocity. Another explanation was given by Heo et al. [22], which was, when the condensation temperature decreased, the thinning of the liquid film due to the difference in the density ratio led to enhanced heat transfer coefficient. Liu et al. [24] attributed this to the vapour phase velocity. When saturation temperature increased the vapour density increased. This leads to a decrease in the vapour phase velocity and the shear stress between vapour and liquid phase leading to thicker liquid film.

Other researchers [24–26] also studied the effect of channel geometry on the heat transfer coefficient. For instance, Matkovic et al. [25] investigated experimentally condensation heat transfer of R134a in a single square minichannel with a hydraulic diameter of 1.18 mm. Their tests were conducted at mass flux ranging from 200 to 800 kg/m² s and saturation temperature of 40 °C. They compared their results with the results of a circular tube of 0.96 mm inner diameter that was conducted by Matkovic et al. [27]. The heat transfer coefficient in the circular tube was corrected by following the correlation of Cavallini et al. [28] since the hydraulic diameter was not the same. They found that, at high mass fluxes, the values of the local heat transfer coefficient in the square and circular channels were very close to each other, while at mass flux of 200 kg/m² s, the heat transfer coefficient in the square channel was higher than that in the circular channel by 20–30%. This enhancement was attributed to the surface tension effect that pulled liquid towards

the channel corners leading to a thinner film at the flat channel sides. Liu et al. [24] investigated condensation heat transfer of R152a in a square and circular minichannel with a hydraulic diameter of 0.952 and 1.152 mm, respectively. Their experiments were conducted at mass flux ranging from 200 to 800 kg/m² s, vapour quality from 0.1 to 0.9 and saturation temperature of 40 and 50 °C. They reported that at low mass fluxes, the heat transfer coefficient in a square channel was higher than that in a circular channel due to the influence of surface tension. The results of Del Col et al. [29] were compared against the study by Bortolin et al. [26], who carried out steady state numerical simulations of R134a in a square minichannel of 1 mm hydraulic diameter. Also, they compared their results with simulations conducted by Da Riva et al. [30], for a circular minichannel. Their tests were conducted at saturation temperature of 40 °C and mass flux of 400 and 800 kg/m² s. They found that at higher mass flux, the heat transfer coefficient was roughly the same in both geometries. At lower mass flux, the heat transfer coefficient in the square channel was higher by 15% due to the surface tension effect.

Some researchers studied the effect of coolant side, the saturation-to-wall temperature difference, on the condensation heat transfer. For example, Matkovic et al. [25] investigated experimentally condensation heat transfer of R134a in a single square minichannel with a hydraulic diameter of 1.18 mm. Water as a coolant was used at inlet temperature of 18.9, 22.4, 25.8, 29.9, and 32.5 °C and refrigerant mass flux of 260 kg/m² s. Their results showed that there was no effect of the saturation-to-wall temperature difference on the experimental local heat transfer coefficient. Similar conclusion was found by Matkovic et al. [27] who studied the effect of inlet coolant temperature and coolant mass flow rate on the local heat transfer coefficient. R134a was tested in a single circular minichannel with inner diameter of 0.96 mm at a mass flux of 417 kg/m² s and saturation temperature of 40 °C. The inlet coolant temperature and coolant mass flow rate were varied from 15 to 29 °C and from 10 to 20.2 kg/hr, respectively. They reported that, the temperature difference had an insignificant effect on the local heat transfer coefficient. The same effect was found when R32 was tested in the same test section at mass flux of 200 kg/m² s and inlet coolant temperature ranging from 19 to 29 °C. Del Col et al. [29] tested R134a in a single square minichannel with side length of 1.18 mm. Their experiments were conducted at a mass flux of 260 kg/m² s, saturation temperature of 40 °C and different inlet coolant temperatures ranging from 19 to 32 °C. They reported that there was no effect of the temperature difference on the local condensation heat transfer coefficient. Kim and Mudawar [6] conducted an experimental study to show the effect of coolant side conditions on the condensation heat transfer coefficient. They studied the condensation heat transfer of FC-72 in square microchannels with a hydraulic diameter of 1 mm. The refrigerant mass flux ranged from 68 to 367 kg/m² s, while the coolant mass velocity ranged from 69 to 138 kg/m² s. They found that the local heat transfer coefficient increased with refrigerant mass flux but decreased slightly with increasing coolant flow rate. This decrease was attributed to the annular liquid film thickness increasing due to an increase in the coolant flow rate. The condensation heat transfer coefficient was more sensitive to variations in refrigerant mass flux than in the coolant flow rate as they reported.

It can be concluded from the previous literature, that in microchannel systems, shear stress and surface tension forces are considered the main forces that affect the heat transfer coefficient. When the shear stress dominates, the heat transfer coefficient increases with increasing mass flux and vapour quality, while in the surface tension dominated regime, it is independent of mass flux. It seems that the heat transfer coefficient increases with decreasing saturation temperature. Also, at low mass fluxes, it is expected that the heat transfer rate in a rectangular channel is higher than that in a circular channel due to the surface tension effect. The coolant side seems to affect only slightly the condensation heat transfer coefficient.

1.3. Pressure drop

The pressure drop is considered an important factor during flow condensation and several numerical and experimental investigations were carried out to understand the effect of operating conditions on the pressure drop. The studies, in Table 1, such as [7,18,21,22,24,31,32] showed that the two phase pressure drop increased with increasing mass flux. Fronk and Garimella [18] attributed the effect of mass flux to the increase in the average velocity as the mass flux increases leading to increased pressure drop.

Other researchers [7,18,24,31] reported the effect of vapour quality on the pressure drop during flow condensation in microchannels. They agreed on that the two phase pressure drop increases as the vapour quality increases. This is due to an increase in the velocity and vapour shear stress as reported by Fronk and Garimella [18].

The effect of saturation temperature on the pressure drop was also investigated by [18,21,22,31,32]. The researchers found that, when the saturation temperature decreased, the two phase pressure drop increased. This was explained by Heo et al. [22] as follows: when the condensation temperature decreased, liquid viscosity increased and vapour density decreased. The decrease in the vapour density results in an increase in the vapour superficial velocity. This led to an increase in the interface shear stress between liquid and vapour and hence the pressure drop.

It seems from the previous studies that the pressure drop during the flow condensation increases with increasing mass flux and vapour quality and decreasing saturation temperature.

1.4. Existing heat transfer correlations

Several correlations were proposed and developed for predicting the condensation heat transfer coefficient in conventional and mini/microchannels. Most of these correlations were proposed for annular flow since this was the main regime during flow condensation. In this section, some of these correlations are described; while the details of each correlation and the dimensionless parameters are presented in Appendix A. Shah [33] proposed a correlation for condensation heat transfer coefficient in different pipe diameters based on dimensionless groups. They developed their correlation for vertical, horizontal and inclined pipes with diameter ranging from 7 to 40 mm. Several fluids such as R11, R12, R22, R113, water, ethanol, methanol, toluene, benzene, and trichloroethylene were included. The operating conditions were set at a mass flux ranging from 10.83 to 210.5 kg/m² s, vapour quality of 0–1, Reynolds number from 100 to 63,000, saturation temperature from 21 to 310 °C and reduced pressure from 0.002 to 0.44. The correlation was exactly the same as the Dittus-Boelter single phase equation but multiplied by a two phase multiplier. The two phase multiplier was correlated as a function of the vapour quality and the reduced pressure. They reported that, the new correlation predicted the data with a MAE of 15.4%. Dobson and Chato [34] conducted an experimental investigation of condensation heat transfer in horizontal pipes with a diameter of 3.14 and 7.04 mm. Different working fluids, namely R12, R22, R134a and R32/R125 were tested at mass flux ranging from 75 to 800 kg/m² s and reduced pressure from 0.21 to 0.57. An annular flow correlation was proposed for the shear dominated regime. In this regime, the heat transfer coefficient depended on the mass flux and quality as they reported. The correlation was similar to the one proposed by Shah [33] but the two phase multiplier was given as a function of the turbulent liquid-turbulent vapour Martinelli parameter. Koyama et al. [35] conducted an experimental investigation on the condensation of R134a in two multiport extruded tubes with a hydraulic diameter of 0.807 and 1.114 mm. One test section consisted of eight channels, while the other one consisted of nineteen channels. In their study, the local pressure drop and heat transfer coefficient were investigated. The results of the local heat transfer coefficient were compared with the correlations of Moser et al. [36] and Haraguchi et al.

[37]. They found that at high mass flux, the correlation of Moser et al. [36] agreed with their results, while the trend was different for the data of low mass flux. Also, they reported that, the correlation of Haraguchi et al. [37] showed a better agreement and a similar trend to the experimental results, when the two phase pressure drop multiplier for the vapour phase in the previous correlation was replaced using the correlation of the Mishima and Hibiki [38]. This is due to the fact that the Mishima–Hibiki correlation was in good agreement with their results. Finally, they proposed their own correlation for the forced convection condensation heat transfer coefficient based on the modification of the correlation of Haraguchi et al. [37]. Cavallini et al. [28] proposed a new model to predict the condensation heat transfer coefficient inside horizontal tubes with inner diameter > 3 mm. Their model was developed from 425 data points including different fluids; R134a, R125, R236ea, R32 and R410A. This model takes into account the dependence (or not) of the heat transfer coefficient on the temperature difference. They compared their model with 5478 data points that were collected from several experiments using different fluids. They reported that, their model predicted the results very well with a mean absolute error of 14%. Wang and Rose [14] conducted a numerical study on flow condensation in non-circular microchannels. They reviewed their original theory that was proposed for different fluids, channel geometries and dimensions. They reported that, for a part of the channel, the local average heat transfer coefficient (averaged along the perimeter) was independent of gravity and shear stress and depended on surface

tension. Therefore, they updated their theory and proposed a new correlation for the surface tension dominated regime. Bohdal et al. [39] investigated experimentally the condensation heat transfer and pressure drop of R134a and R404A in stainless steel mini pipes with inner diameter of 0.31–3.3 mm. Their experiments were conducted at mass flux ranging from 100 to 1300 kg/m² s, vapour quality of 0–1 and saturation temperature of 20–40 °C. They reported that the correlation of Akers et al. [40] and Shah [33] could be used within a limited range of inner diameter and mass flux. For example, at a mass flux $G < 400\text{--}600\text{ kg/m}^2\text{ s}$ and diameter less than 1.4 mm, the correlation of Akers et al. [40] was in a good agreement with their results. At a mass flux higher than 600 kg/m² s, better results were found when using the correlation of Shah [33]. Thus, they proposed their own correlation to calculate the local condensation heat transfer coefficient. Park et al. [41] investigated experimentally condensation heat transfer of R1234ze(E), R134a and R236fa in vertical multiport tubes. Their test section consisted of seven rectangular aluminium minichannels with a hydraulic diameter of 1.45 mm. In their experiments, the mass flux ranged from 50 to 260 kg/m² s, and the heat transfer coefficient was calculated locally and compared with other correlations, such as Koyama et al. [42], Cavallini et al. [43] and Moser et al. [36]. Their results were higher at high Nusselt number and lower at low Nusselt number than those predicted by the past correlations. However, their results were predicted quite well at the mid-range. Accordingly, they modified the correlation of Koyama et al. [42], which was proposed as a

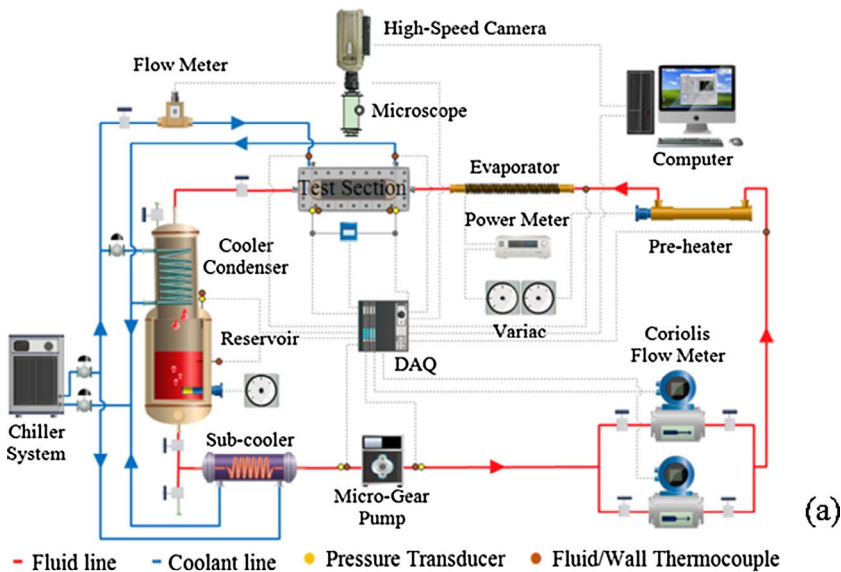


Fig. 1. (a) Schematic diagram of the experimental facility and (b) photograph of the test rig.

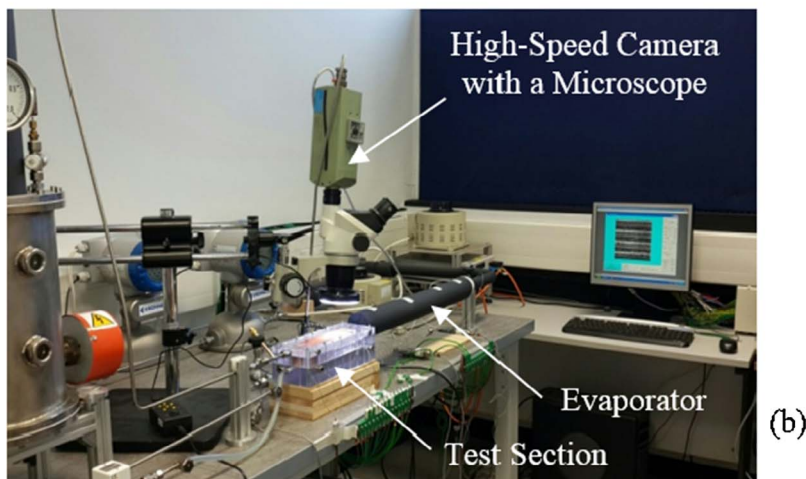


Table 2
Thermophysical properties of HFE-7100 at 1 bar.

i_{lg} (kJ/kg)	ρ_l (kg/m ³)	ρ_g (kg/m ³)	k_f (W/m K)	C_p (kJ/kg K)	σ (N/m)
111.661	1373	9.575	0.06206	1.157	0.0136

Table 3
Experimental operating conditions.

Refrigerant	HFE-7100
System pressure (bar)	1
Saturation temperature (°C)	59.63
Mass flux (kg/m ² s)	48 – 126
Inlet quality	0.95 – 1
Coolant	Water
Inlet temperature (°C)	20 – 40
Flow rate (L/min)	0.5 – 1.1

combination of gravity controlled and forced convection to include the effect of non-circular channel geometries. The modification included optimising the empirical constant in the original correlation by fitting the experimental data and adjusting this constant. Their modified correlation showed a good agreement with the experimental results for all fluids. Kim and Mudawar [44] presented a new universal approach to calculate the condensation heat transfer coefficient in single and multi-channels. They collected 4045 data points from 28 sources for circular and rectangular channels. The consolidated database consisted of different fluids (R134a, R12, R22, R123, R1234ze(E), R1234yf, R245fa, R236fa, R404, R32, R410A, R600a, FC-72, CO₂ and methane), hydraulic diameter ranging from 0.424 to 6.22 mm, mass flux from 53 to 1403 kg/m² s, Reynolds number from 276 to 89798, vapour quality of 0–1 and reduced pressure from 0.04 to 0.91. They proposed two correlations, one for annular flow and another for slug and bubbly flows. They reported that, the consolidated database was predicted very well with an overall mean absolute error of 16.0%. Shah [45] proposed a correlation of condensation heat transfer coefficient in horizontal mini/microchannels for a hydraulic diameter equal or less than 3 mm. They collected 67 data sets from 31 sources for 13 different fluids (R134a, R22, R32, R152a, R1234ze(E), R245fa, R410A, R1234fa, FC-72, propane, butane, water and CO₂) with a hydraulic diameter ranging from 0.1 to 2.8 mm. Their correlation was verified with data sets in single and multi-channels of various shapes at mass flux ranging from 20 to 1400 kg/m² s, aspect ratio from 0.14 to 13.9 and reduced pressure from 0.0055 to 0.94. They developed their correlation by modifying the correlation of Shah [46]. In their correlation, the heat transfer coefficient was proposed for three regions, namely I, II, and III, see Appendix A. The boundaries between these regimes can be identified based on the dimensionless vapour velocity. They reported that, the new correlation predicted 1017 data points with a MAE of 15.5%.

Although several experimental research projects have been conducted in flow condensation in microchannels, few of them were carried out in rectangular multi-microchannels using fluids that are compatible with cooling electronic components with low environmental impact. Moreover, there are only a few studies that have been carried out to determine the condensation heat transfer coefficient locally, especially in micro scale. 3M Novec Engineering fluid HFE-7100 is a recommended fluid for electronics cooling due to its low global warming potential and its high dielectric strength. The saturation temperature of this fluid is 60 °C at atmospheric pressure, which makes it suitable for cooling electronics that require surface temperature below 85 °C or power electronics that require temperature below

125 °C. To the best of the authors' knowledge there are no data available in the literature for this fluid under flow condensation in single or multi-microchannels. Therefore, the objective of this study was to investigate experimentally the condensation heat transfer of HFE-7100 in horizontal rectangular multi-microchannels with a hydraulic diameter of 0.57 mm. Local heat transfer measurements with flow visualization were conducted, to understand the condensation phenomena clearly at micro scale. The effect of mass flux, local vapour quality, inlet coolant temperature and coolant flow rate on the local condensation heat transfer coefficient were investigated. All experiments were performed at mass flux ranging from 48 to 126 kg/m² s, saturation temperature of 60 °C, inlet coolant temperature from 20 to 40 °C and coolant flow rate from 0.5 to 1.1 L/min. Several existing heat transfer correlations and flow pattern maps were evaluated using the current experimental data.

2. Experimental system

2.1. Flow loop

Fig. 1(a) and (b) show a photograph and a schematic diagram of the experimental facility, respectively. The test rig consists of an auxiliary cooling loop and a test loop. The auxiliary cooling loop is a re-circulating chiller system (Cole-Parmer Polystat chiller) with a cooling capacity of 2900 W. The test loop starts from a liquid reservoir, which is a stainless steel cylindrical vessel with a total volume of 9 L. The cooling coil condenser was mounted on the top side of the reservoir and an electric immersion heater of 1500 W was inserted to control the temperature inside the reservoir and the system pressure during the experiments. A Variac model CMV15E-1 was used to control this heater. Two T-type thermocouples and one pressure transducer were fitted to the reservoir to detect vapour, liquid temperature and fluid pressure. A tube-in-tube heat exchanger (sub-cooler) was located after the reservoir

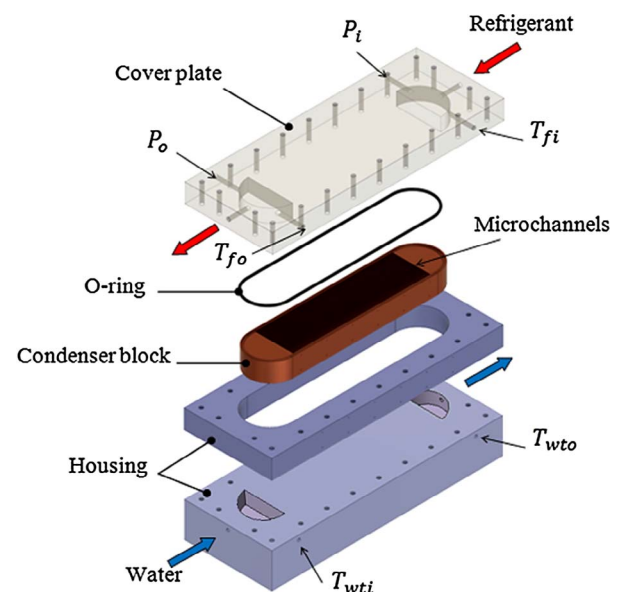


Fig. 2. Test section construction.

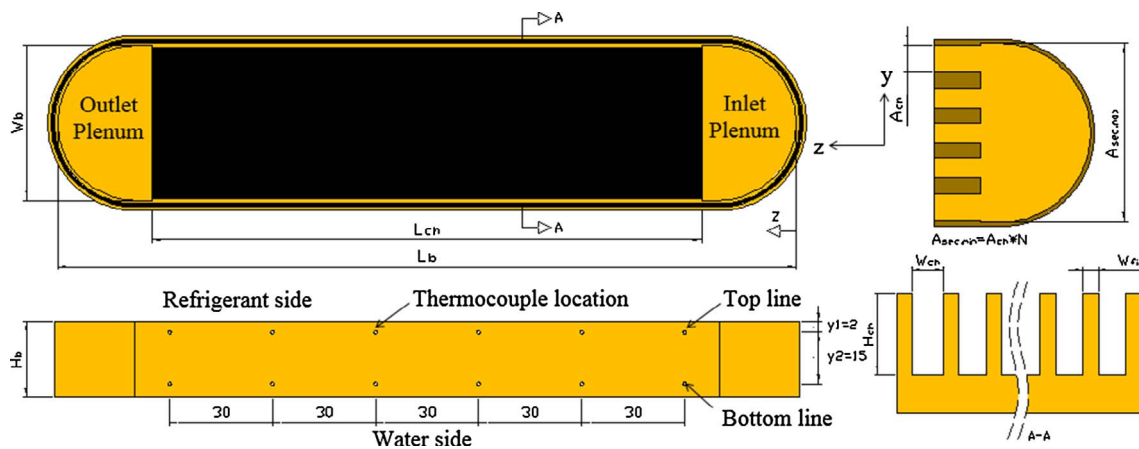


Fig. 3. Condenser details, dimensions in [mm].

and before the pump. A micro-gear pump (Cole-Parmer model TW-74014-25) with a flow rate ranging from 38.4 to 2304 mL/min at a motor speed ranging from 60 to 3600 rpm was used to drive the fluid around the loop. Two KROHNE model Optimass 3300 C Coriolis flow meters, one for low mass flow rate up to 5 kg/hr and another one for high rate ranging from 5 to 130 kg/hr, were installed in the rig. A pre-heater of 1500 W was used and controlled by a Variac model CMV5E-1, to control the fluid condition during the experiments. Moreover, a stainless steel tubular evaporator heated by a rope heater of 500 W was located after the pre-heater. Both the pre-heater and the evaporator were used to create slightly superheated vapour at the inlet of the microchannel condenser. A Variac model CMV15E-1 was used to control the power of the evaporator and to control the exit vapour quality. Both the pre-heater and the tubular evaporator were well insulated using thermal insulation strips. A Hameg HM8115-2 power meter with accuracy of $\pm 0.4\%$ was used to measure the power supply to the heat sources. The test section (microchannel condenser) was mounted after the tubular evaporator and the Omega turbine flow meter with a range of 0.3–5 L/min was used to measure the coolant flow rate before entering the condenser. A set of T and K-type thermocouples and pressure transducers are located at different locations in the rig for measuring the fluid condition during the experiments. A Phantom digital high-speed camera with an image resolution of 512×512 pixel at 1000 fps was fitted on a microscope to capture the flow patterns inside the test section. A National Instruments Data Acquisition System (DAQ) was used for recording and processing all the signals from the measuring instruments that were connected to a computer. The data logger frequency is 1 kHz that means 1000 data is recorded per second. Once steady state conditions were established, the data were taken for 2 min and averaged.

In this study, HFE-7100 was chosen as the working fluid due to a number of reasons. It is a dielectric fluid and at system pressure of 1 bar, the saturation temperature is 60 °C. Therefore, this fluid is compatible with cooling electronics components at surface temperature

Table 4
The details of microchannel condenser.

HFE-7100 side					
H_{ch} (mm)	W_{ch} (mm)	W_{fin} (mm)	D_n (mm)	β	
1.0	0.4	0.1	0.57	0.4	
L_{ch} (mm)	A_{ht} (m ²)	$W_b \times L_b$ (mm)	H_b (mm)	N	
160	0.035	45 × 216	22	90	
Water side					
H_{ch} (mm)	W_{ch} (mm)	W_{fin} (mm)	L_{ch} (mm)	N	
2	2	1	160	15	

below 80 °C. Moreover, this fluid has low Ozone depletion potential (0.00), low global warming potential (320 over 100-year) and low atmospheric lifetime (4 years). Therefore, HFE-7100 is considered environmentally friendly and good choice if it is compared with other refrigerants. Also, this fluid is compatible with a wide range of metals and plastics. So, it can be used for commercial applications without any limitations. Despite the aforementioned advantages of this fluid, it has a great affinity to absorb dissolved air. Thus, in the present study, degassing was conducted every day before running the test by boiling the liquid vigorously inside the tank for about one hour. The cooling coil condenser was switched on while the liquid was boiling in the reservoir. Thus, the vapour condenses back to the reservoir while the gases remain trapped in the top of the condenser and are released to the ambient by opening a ventilation valve. This process ends when the saturation pressure (corresponding to the measured temperature in the reservoir) equals the measured pressure in the reservoir. A summary of the thermophysical properties of HFE-7100 at atmospheric pressure is presented in Table 2 and the experimental conditions are shown in Table 3. In calculations conducted in this study, all properties of HFE-7100 were obtained from the EES software.

2.2. Test section

The test section consists of three parts as shown in Fig. 2, namely the cover plate, the housing and the condenser block. Both the cover plate and the housing were made of polycarbonate to minimize the heat loss during the experiments. The cover plate was made of a transparent sheet and allows viewing the flow patterns inside the channels. The inlet/outlet plenum was formed in this part and six tapping holes were drilled into the cover plate to connect the fluid inlet/outlet thermocouples, inlet/outlet pressure transducers and fluid inlet/outlet port. An O-ring seal was inserted into a slot between the cover plate and the condenser block to prevent any leakage. This plate was clamped on the housing and fitted with a set of screws. Twelve holes of 0.6 mm

diameter were drilled into the housing. The purpose of these holes is to pass thermocouple wires through the housing. The condenser block was made of oxygen free copper using high precision micro-milling machine (Kern HSPC-2216) with a speed rotation of 12,000 rpm and cutting feed rate of 300 mm/min. This block consists of microchannels and inlet/outlet plenum on both faces. In this study, a counter-current flow condenser was tested with overall dimensions of 22 mm height, 51 mm width and 221 mm length. At the refrigerant side, ninety microchannels of 1 mm height, 0.4 mm width and 0.1 mm fin thickness were manufactured while at the coolant side, fifteen square channels with side length of 2 mm and fin thickness 1 mm were milled. Twelve holes of 0.6 mm diameter and 20 mm length were drilled to insert the thermocouples into this block. Twelve K-type thermocouples were inserted in two rows, 6 at the top and 6 at the bottom, to measure the temperature gradient during the condensation and consequently the local heat flux. Four T-type thermocouples were used for measuring the inlet and outlet temperatures of the refrigerant and the inlet and outlet of the coolant side. Also, two pressure transducers with a measuring range of 0–6.9 bar and differential pressure transducer with a measuring range from 0 to 0.35 bar were connected to the test section to measure inlet/outlet pressure and the total pressure drop along the condenser. The details of the condenser block are presented in Fig. 3 and Table 4.

3. Data reduction

3.1. Single phase

The pressure drop along the channel is calculated from the equation below.

$$\Delta P_{ch} = \Delta P_{meas} - (\Delta P_{ip} + \Delta P_{sc} + \Delta P_{se} + \Delta P_{op}) \quad (1)$$

where ΔP_{meas} is the total measured pressure drop between the inlet and outlet plena, ΔP_{ip} and ΔP_{op} are the pressure drop due to the change in flow direction by 90° in the inlet and outlet plena respectively, ΔP_{sc} is the sudden contraction pressure drop at the channel inlet and ΔP_{se} is the sudden expansion pressure drop at the channel outlet. The values of each pressure drop component in Eq. (1) are found from the equations below as described by Remsburg [47].

$$\Delta P_{ip} = K_{90} * \frac{1}{2} G_p^2 * v_l \quad (2)$$

$$\Delta P_{op} = K_{90} * \frac{1}{2} G_p^2 * v_l \quad (3)$$

$$\Delta P_{sc} = \frac{1}{2} G_{ch}^2 * v_l * [1 - \alpha^2 + 0.5(1 - \alpha)] \quad (4)$$

Table 5

The uncertainty ranges for the measured and calculated variables.

Parameter	Uncertainty
Temperature T-type	± 0.024 K
Temperature K-type	± 0.12 K
Inlet pressure transducer	± 0.46 kPa
Outlet pressure transducer	± 0.37 kPa
Differential Pressure	± 0.08%
Refrigerant mass flow rate	± 0.1%
Coolant mass flow rate	± 1%
Local vapour quality	± 0.012–0.07[-]
Heat transfer coefficient	± 3.6–21%
Mass flux	± 0.26–0.7 kg/m ² s
Heat flux	± 3.8–16%
Fanning friction factor	± 1.46–1.52%
Average Nusselt number	± 7.6–11.9%

$$\Delta P_{se} = \frac{1}{2} G_{ch}^2 * v_l * \left[\frac{1}{\alpha^2} - 1 + (1 - \alpha)^2 \right] \quad (5)$$

The loss coefficient of the 90 degree turns (K_{90}) is approximately 1.2 as suggested by Phillips [48] and the value of the area ratio (α) is found from the minimum/maximum cross sectional area, see Fig. 3. Equation (6) below is used to calculate the experimental fanning friction factor while the Reynolds number Re , the hydraulic diameter D_h and the mass flux in the channel G_{ch} can be determined from Eq. (7), (8), and (9), respectively:

$$f_{exp} = \frac{\Delta P_{ch} * D_h}{2 L_{ch} * v_l * G_{ch}^2} \quad (6)$$

$$Re = G_{ch} * D_h / \mu_l \quad (7)$$

$$D_h = 2 H_{ch} * W_{ch} / (H_{ch} + W_{ch}) \quad (8)$$

$$G_{ch} = \frac{\dot{m}}{(W_{ch} * H_{ch}) * N} \quad (9)$$

where L_{ch} , v_l , H_{ch} , W_{ch} , \dot{m} and N are the channel length, liquid specific volume, channel height, channel width, fluid mass flow rate and number of channels, respectively. The local single phase heat transfer coefficient is calculated using Eq. (10).

$$h_{sp(z)} = \frac{q''_{b(z)} * (W_{ch} + W_{fin})}{(T_{f(z)} - T_{wi(z)}) * (W_{ch} + 2\eta * H_{ch})} \quad (10)$$

where $q''_{b(z)}$, W_{fin} , $T_{f(z)}$, $T_{wi(z)}$ and η are the local base heat flux, fin width, local fluid temperature, local internal surface temperature and the fin

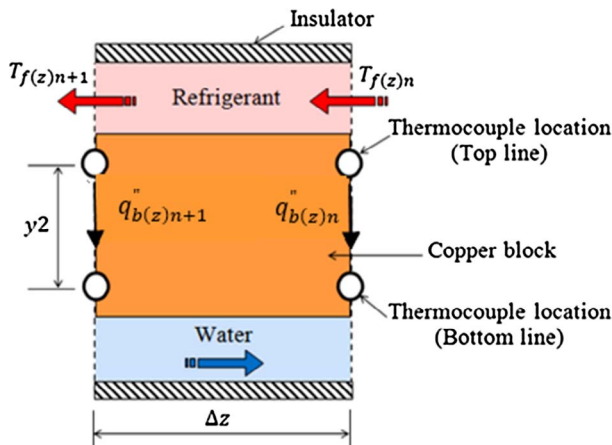


Fig. 4. Thermal element of the condenser.

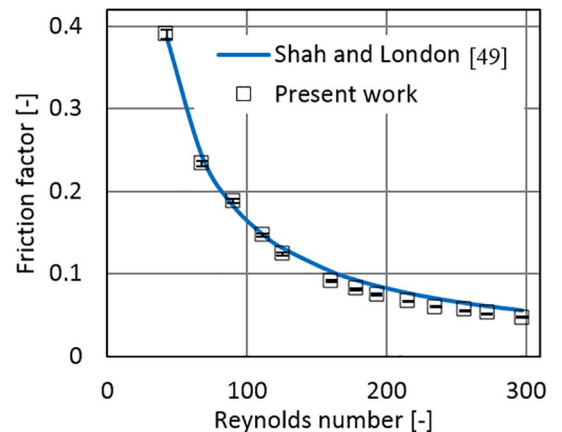


Fig. 5. Experimental Fanning friction versus Reynolds number.

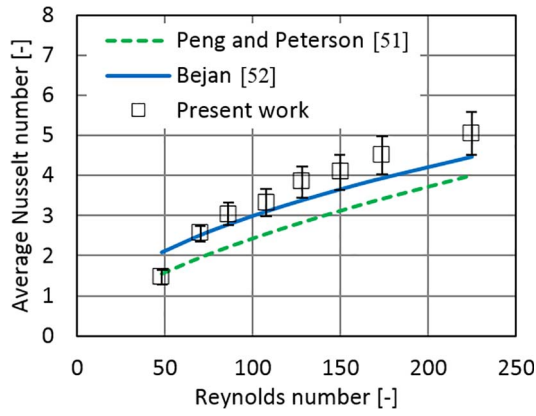


Fig. 6. Average Nusselt number versus Reynolds number.

efficiency, respectively. The local base heat flux during the experiments is calculated directly from the vertical temperature gradient at six axial locations, see Eq. (11) below. It is worth mentioning that when the heat transfer rate is measured at both the refrigerant and water sides, the percentage of the heat loss varied from 0.57% to 12.8%.

$$q''_{b(z)} = k_{cu} * \frac{(T_{T(z)} - T_{B(z)})}{y_2} \quad (11)$$

where k_{cu} , $T_{T(z)}$, $T_{B(z)}$ and y_2 are the thermal conductivity of copper, the local thermocouple temperature at the top line, the local thermocouple temperature at the bottom line and the vertical distance between thermocouples, respectively, see Fig. 3 for more details. The condenser block is divided into thermal elements as shown in Fig. 4. The local fluid temperature was calculated using an energy balance by Eq. (12) below.

$$T_{f(z)n} = T_{f(z)n+1} + \frac{\left[\frac{q''_{b(z)n} + q''_{b(z)n+1}}{2} \right] * W_b * \Delta z}{\dot{m} * cp_f} \quad (12)$$

where $T_{f(z)n+1}$, W_b , cp_f and Δz are the local outlet fluid temperature at the thermal element, base width, the specific heat at constant pressure and the axial distance between thermocouples, respectively. As mentioned above, the inlet and outlet plena were formed in the condenser block. Therefore, the best fit equation of the curve resulting from plotting the local base heat flux versus axial distance was used to calculate the base heat flux at any axial location. This approach was adopted by Ma et al. [8] and Jiang et al. [11].

$$q''_b = f(z) \quad (13)$$

The above fitting equation is a third or fourth order polynomial and its coefficients changes with the experimental operating conditions. The base heat flux at the inlet and outlet plena is found from Eq. (13) at the axial location (z) of 5 and 205 mm, respectively. The local internal surface temperature and the fin efficiency in Eq. (10) are determined as follows:

$$T_{wi(z)} = T_{T(z)} + \frac{q''_{b(z)} * y_1}{k_{cu}} \quad (14)$$

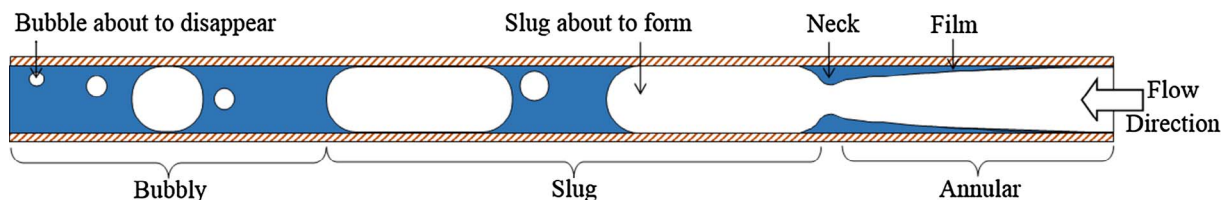


Fig. 7. Condensation flow structure.

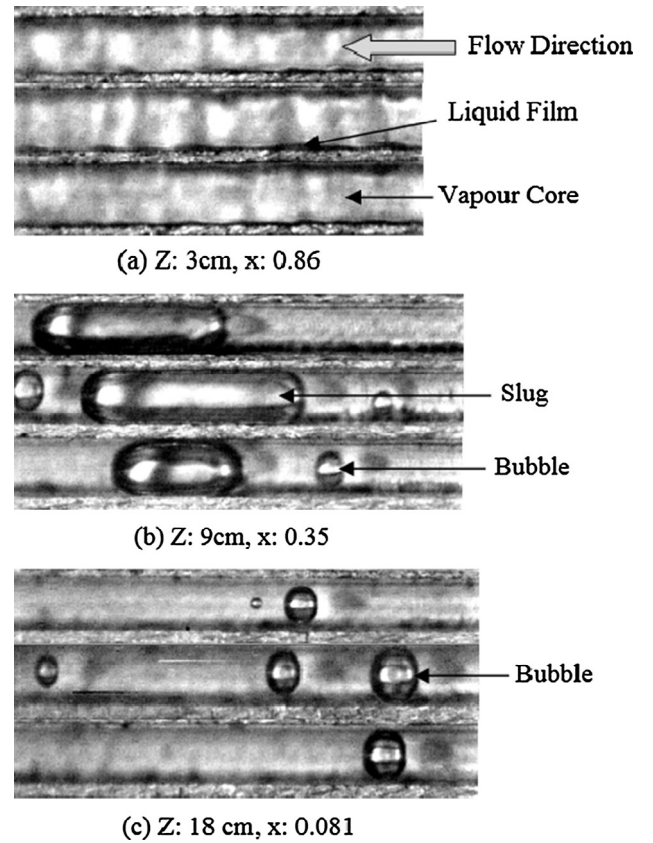


Fig. 8. Flow patterns along the condenser at mass flux of 108 kg/m² s, coolant flow rate of 0.8 L/min and inlet coolant temperature of 25 °C with corresponding local quality: (a) Annular (b) Slug (c) Bubbly.

$$\eta = \frac{\tanh(m * H_{ch})}{m * H_{ch}} \quad (15)$$

$$m = \sqrt{\frac{2 * h_{sp(z)}}{k_{cu} * W_{fin}}} \quad (16)$$

where y_1 is the vertical distance between the thermocouple at the top line and the channel bottom, which is 2 mm. The average heat transfer coefficient can be calculated from the equation below.

$$\bar{h} = \frac{1}{L} \int_0^L h_{(z)} dz \quad (17)$$

where L is the span between the first and the last thermocouple. The average Nusselt number is calculated using Eq. (18).

$$\overline{Nu} = \frac{\bar{h} * D_h}{k_f} \quad (18)$$

3.2. Two phase

The local two phase heat transfer coefficient is calculated using Eq. (19) below.

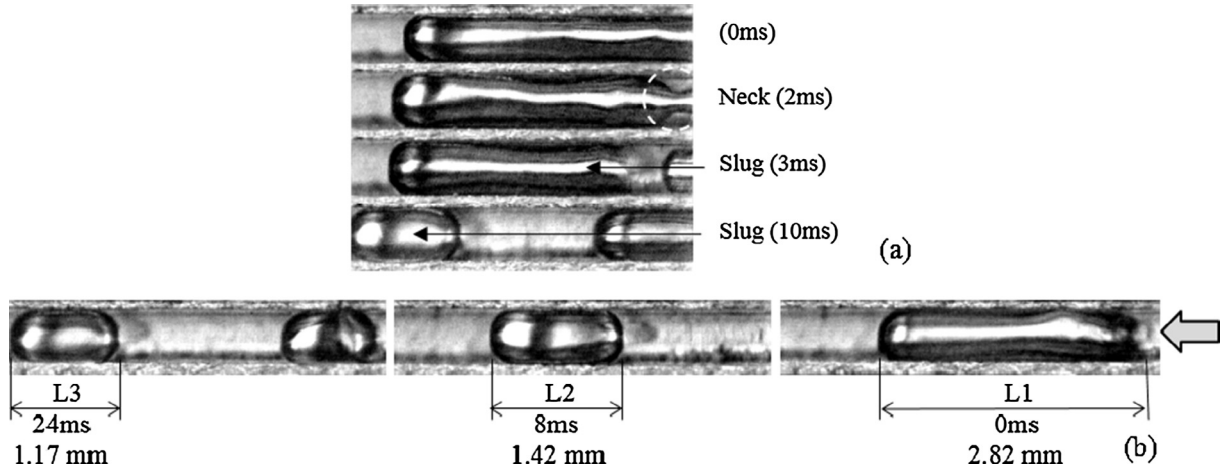


Fig. 9. Sequence of pictures at a local quality of 0.35 for (a) The necking phenomenon and the slug formation (b) Bubble length after the neck region.

$$h_{tp(z)} = \frac{q_{b(z)}'' * (W_{ch} + W_{fin})}{(T_{sat(z)} - T_{wt(z)}) * (W_{ch} + 2\eta * H_{ch})} \quad (19)$$

The local saturation temperature $T_{sat(z)}$ was determined using the local saturation pressure, which is calculated using the following equation:

$$P_{sat(z)} = P_i - (P_i - P_{sat(z,sp)}) * \left(\frac{z}{L_{ch} - L_{sp}} \right) \quad (20)$$

where P_i and L_{sp} are the inlet pressure and the length of the condenser in the single phase region, respectively. The local saturation pressure at the onset of the single phase region $P_{sat(z,sp)}$ was found from the following equation:

$$P_{sat(z,sp)} = P_o + \frac{2f * G_{ch}^2 * L_{sp}}{\rho_l * D_h} \quad (21)$$

where P_o , f and ρ_l are the outlet pressure, the fully developed fanning friction factor and the liquid density, respectively. According to the procedure that was described by Shah and London [49], the entrance length for the present study is 3.56 mm at maximum Reynolds number of 120.3. This means that just 2.2% of the channel length was in the developing region. Therefore, the friction factor for laminar fully developed flow is calculated from Eq. (22) as proposed in [49].

$$f = (24(1 - 1.355\beta + 1.946\beta^2 - 1.7012\beta^3 + 0.9564\beta^4 - 0.2537\beta^5)) / Re \quad (22)$$

The aspect ratio β is defined as follows:

$$\beta = W_{ch} / H_{ch} \quad (23)$$

The single phase length can be calculated from the following equation:

$$L_{sp} = \frac{\dot{m} * cp_l * (T_{sat(z,sp)} - T_{fo})}{\bar{q}_b'' * W_b} \quad (24)$$

The local saturation temperature at the onset of the single phase region $T_{sat(z,sp)}$ is found from the local saturation pressure at the onset of the single phase region $P_{sat(z,sp)}$. Therefore, an iteration process was used

between Eq. (21) and (24) to find the single phase length. The average base heat flux \bar{q}_b'' is calculated from Eq. (25) while the local vapour quality is calculated from Eq. (26) below.

$$\bar{q}_b'' = \frac{1}{L} \int_0^L q_{b(z)}'' dz \quad (25)$$

$$x_{(z)n+1} = x_{(z)n} - \frac{\left[\frac{q_{b(z)n}'' + q_{b(z)n+1}''}{2} \right] * W_b * \Delta z}{\dot{m} * i_{lg(z)}} \quad (26)$$

where $i_{lg(z)}$ is the latent heat of vaporization at the local saturation pressure. The inlet vapour quality at the condenser was calculated from an energy balance in the tubular evaporator and the pre-heater as follows:

$$x_i = \frac{Q}{\dot{m} * i_{lg}} + \frac{cp_l * (T_{fi} - T_{sat})}{i_{lg}} \quad (27)$$

where Q , T_{fi} , T_{sat} and i_{lg} are the electric power supplied to the evaporator and the pre-heater, the fluid temperature at the inlet of the pre-heater, the saturation temperature and the latent heat of vaporization estimated at the inlet pressure of the pre-heater, respectively.

3.3. Uncertainty analysis

The experimental uncertainty analysis was conducted using the procedures described by Coleman and Steele [50]. Table 5 summarizes the uncertainties of the measured and calculated variables.

4. Results and discussion

4.1. Single phase validation

Single phase experiments were conducted for the counter-current flow condenser before the flow condensation tests to validate the experimental measurement system. Several experiments were carried out at system pressure of 1 bar, inlet refrigerant temperature ranging from

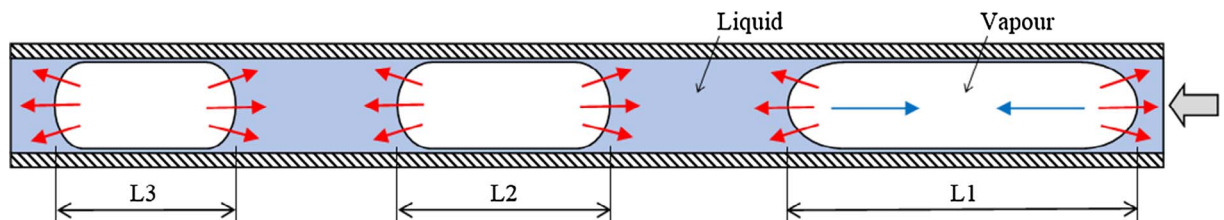


Fig. 10. Schematic diagram of a vapour slug after the neck region (Top view), blue arrows indicate surface tension effect and red condensation of vapour.

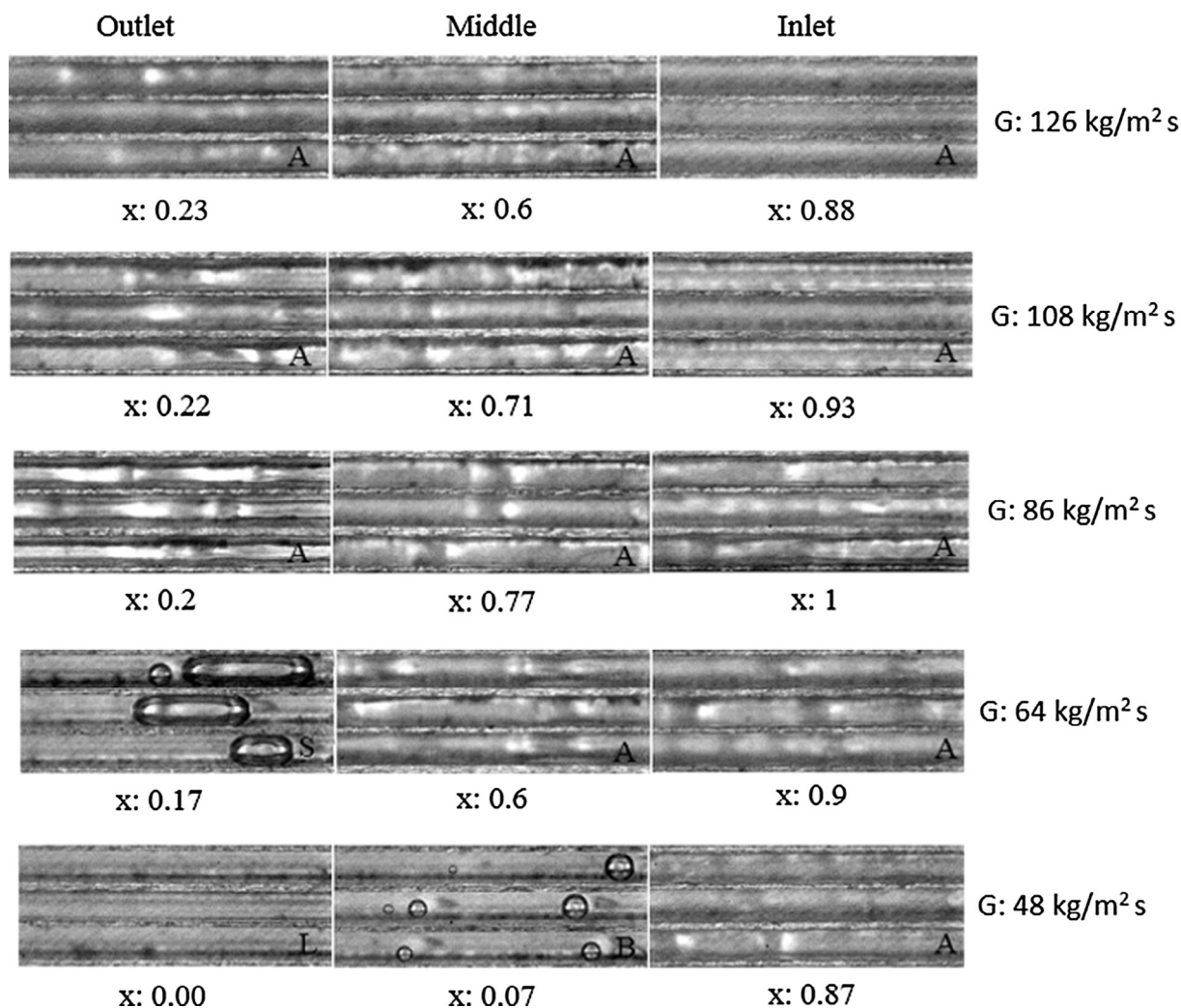


Fig. 11. Flow patterns at different mass fluxes, coolant flow rate of 0.5 L/min and inlet coolant temperature of 40 °C with corresponding local quality. (A) Annular (S) Slug (B) Bubbly (L) Liquid.

41 to 44 °C, inlet coolant temperature of 17.5 °C and coolant flow rate of 0.3 L/min. Different mass fluxes ranging from 48 to 341.2 $\text{kg/m}^2\text{s}$ were chosen. Several existing correlations were compared with the present results as presented in Appendix B. Fig. 5 shows the experimental Fanning friction factor versus Reynolds number. The results show a good agreement with the correlation of Shah and London [49] for fully developed laminar flow.

The results of the Nusselt number versus Reynolds number are shown in Fig. 6. They were compared with the correlation of Peng and Peterson [51] and Bejan [52], which were proposed for laminar flow in non-circular channels. It is shown from this figure that the trend of the experimental results is similar to that of Peng and Peterson [51] and Bejan [52], being closer to the latter. It can be concluded from the previous results, the single phase experiments confirmed the validation of the rig.

4.2. Two phase flow patterns

Flow visualization was carried out at three different locations; channel inlet, middle and outlet to capture flow patterns during the condensation experiments. Fig. 7 shows a schematic drawing for the flow structure during the condensation experiments observed in the present study. It shows that the fluid enters the channels at high vapour quality where the flow pattern is annular. This regime is characterized by a vapour core surrounded by a thin liquid film. The annular flow gets

distorted at the neck region due to the condensation process along the channels. When the liquid edges in the neck region join up, a vapour slug separates from the vapour core. With further condensation along the channel, the length of the vapour slug decreases until bubbly flow develops. The typical photographs of the annular, slug and bubbly flow patterns are depicted in Fig. 8(a), (b) and (c), respectively. Fig. 9(a) illustrates the sequence of pictures that show the neck region at which the vapour slug is formed. It was observed that, after slug separation, the slug length decreases suddenly and after 10 ms, this reduction occurs gradually. This reduction in the slug length is due to the condensation process and is illustrated in Fig. 9(b). This figure depicts the variation in the bubble length with time during the necking process for 4 mm distance. At time of 0 ms (slug formation or separation), the bubble length was 2.82 mm, which decreased to 1.42 mm after 8 ms and decrease further to 1.17 mm after 24 ms. Accordingly, after slug separation, the bubble length decreased by 49.6% after 8 ms while it decreased by 17.6% after 16 ms. In other words, the slug length decreases rapidly in the early stage of slug formation then it decreases slowly. This could be explained as follows: when the slug separates from the vapour core, the forces that affect the bubble change abruptly and become imbalanced. Surface tension force tries to pull the bubble into the spherical shape. This leads to a rapid change in the slug size. It is obvious that, this rapid reduction (49.6%) is due to the effect of both condensation process and surface tension, while the low reduction (17.6%) is due to the condensation as shown in Fig. 10. It is worth

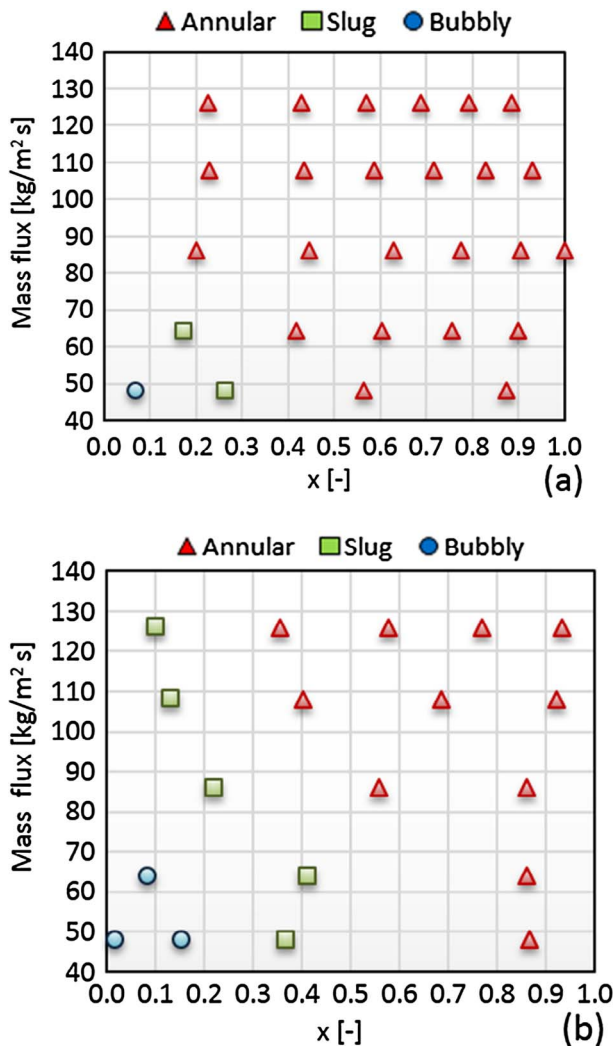


Fig. 12. Flow patterns map at five mass fluxes ranging from 48 to 126 kg/m² s, coolant flow rate of 0.5 L/min and two different inlet coolant temperatures: (a) 40 °C (b) 20 °C.

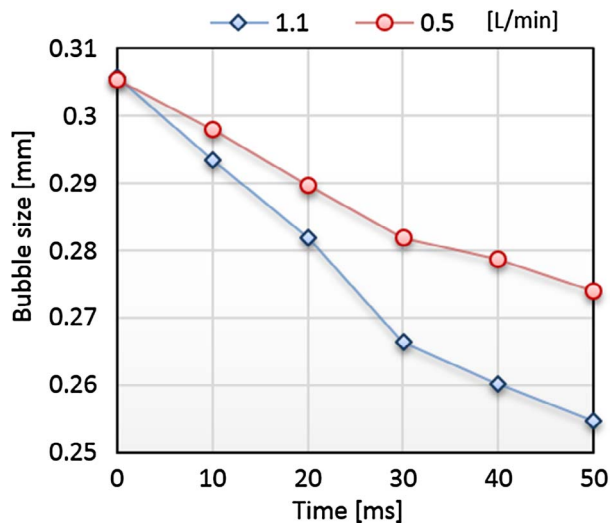


Fig. 13. Bubble size reduction rate at mass flux of 108 kg/m² s, inlet coolant temperature of 20 °C and coolant flow rate of 0.5 and 1.1 L/min.

mentioning that, the above phenomenon was not reported by other studies. Slug flow is characterized by a cylindrical bubble, its size equals to the channel width, followed by trailing bubbles. This slug begins to shrink and decrease in size along the axial direction due to the heat transfer from the vapour slug to the liquid. After that, bubbly flow forms which is characterized by numerous bubbles flowing in the liquid phase. Some of these bubbles reach the channel width, while others become smaller. Then these bubbles shrink along the channels and submerge in the condensate.

Fig. 11 depicts the effect of mass flux on flow patterns at three axial locations (near inlet, middle and near outlet) and coolant flow rate of 0.5 L/min and inlet coolant temperature of 40 °C. It demonstrates that the annular flow is the dominant flow regime at high mass fluxes. This seems clear at mass flux ranging from 86 to 126 kg/m² s. However, at low mass fluxes $G = 64$ and 48 kg/m² s, other flow patterns were also observed such as slug and bubbly flow.

The previous regimes were presented as a flow pattern map using two coordinates namely; mass flux and vapour quality as shown in Fig. 12. In Fig. 12(a), the inlet coolant temperature was 40 °C while the data in Fig. 12(b) were for inlet coolant temperature 20 °C. It seems that annular, slug and bubbly flow regimes shift to the right, i.e. higher quality, when the inlet coolant temperature decreases. This could be due to an increase in the heat transfer rates, when the inlet coolant temperature decreases. Increased heat transfer rates may lead to a decrease in vapour length along the channels and hence the appearance of slug and bubbly flow. Fig. 13 shows the reduction in the bubble diameter at mass flux of 108 kg/m² s, inlet coolant temperature of 20 °C and two different coolant flow rates of 0.5 and 1.1 L/min. The bubble reduction size can be found based on the sequence of pictures for a condensing bubble as shown in Fig. 14. It is obvious that, the bubble size decreases with time due to the heat transfer from the bubble to the surrounding liquid. The size reduction rate is higher at the higher coolant flow rate of 1.1 L/min compared to the 0.5 L/min (higher heat transfer rate). This confirms that the bubble reduction size decreases with increasing coolant flow rate.

The present results are compared with two flow pattern maps reported in the literature. The first flow pattern map is for conventional size channels and the second for mini and microchannels. The flow pattern maps of Cavallini et al. [53] were used for conventional size channels. They presented their maps for several fluids, R22, R134a, R125, R32, R236ea, R407C and R410A, in 8 mm inner diameter using the Martinelli parameter and dimensionless gas velocity as coordinates. Their experiments were conducted at saturation temperature ranging from 30 to 50 °C and mass flux from 100 to 750 kg/m² s. Fig. 15 depicts the comparison with this map and it is obvious that this map is only able to predict the annular flow. They proposed the transition criteria of flow regimes as follows: $J_G > 2.5$ for annular flow, $J_G < 2.5$ and $X_{tt} < 1.6$ for stratified flow, and $J_G < 2.5$ and $X_{tt} > 1.6$ for slug flow.

Nema et al. [54] proposed a flow pattern map for R134a in mini and microchannels with a hydraulic diameter ranging from 1 to 4.91 mm at vapour quality ranging from 0 to 1 and mass flux from 150 to 750 kg/m² s. Two different channel geometries were tested namely; circular and rectangular. They used a vapour phase Weber number versus turbulent-turbulent Martinelli parameter to present their map. Their study showed that, for $Bo \leq Bo_{cr}$, the transition criteria of flow regimes are as follows: (1) $We_g > 700$ and $X_{tt} < 0.175$ for mist flow (MF), (2) $We_g < 35$ and $X_{tt} > 0.3521$ for dispersed flow (DF), (3) $We_g \leq 35$ or $We_g < 35$ and $X \leq 0.3521$ for annular flow (AF), if the previous flows are not present, (4) $6 \leq We_g < 35$ and $X_{tt} > 0.3521$ for intermittent (slug or plug)-annular flow (I-AF), if dispersed flow is not present, (5) $We_g < 6$ and $X_{tt} > 0.3521$ for intermittent flow (IF), if dispersed flow is not present. Fig. 16 shows a comparison between their map and the present flow patterns. Mist and dispersed flow were not observed during the current experiments and hence these regimes were not presented in this map. It seems that the annular flow is well predicted by this map, while their map is not able to predict the slug and bubbly flow.

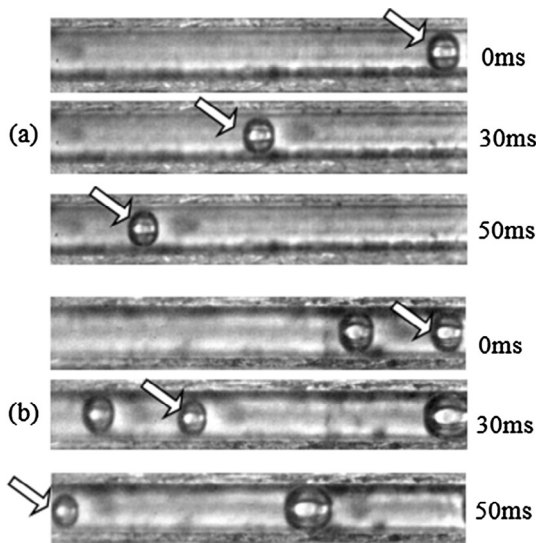


Fig. 14. Condensing bubble at mass flux of 108 kg/m² s, inlet coolant temperature of 20 °C and coolant flow rate: (a) 0.5 (b) 1.1 L/min.

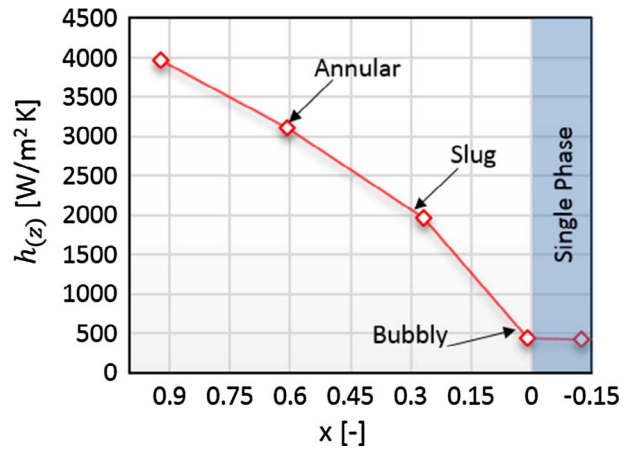


Fig. 17. Local heat transfer coefficient versus local vapour quality at mass flux of 108 kg/m² s, coolant flow rate of 1.1 L/min, and inlet coolant temperature of 20 °C.

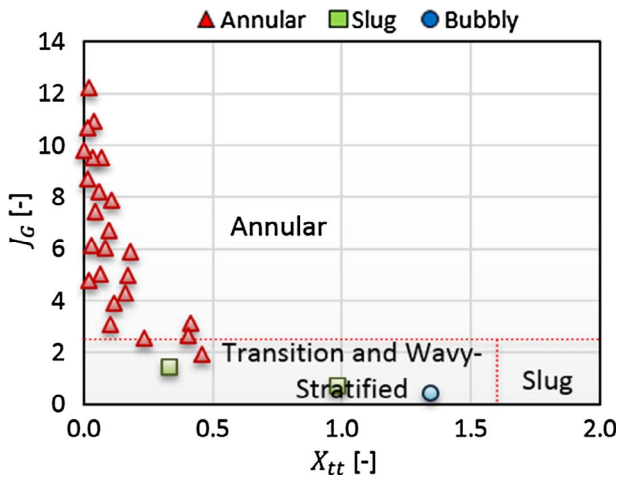


Fig. 15. Comparison of the present results with the proposed map of Cavallini et al. [53] at a coolant flow rate of 0.5 L/min and inlet coolant temperature of 40 °C.

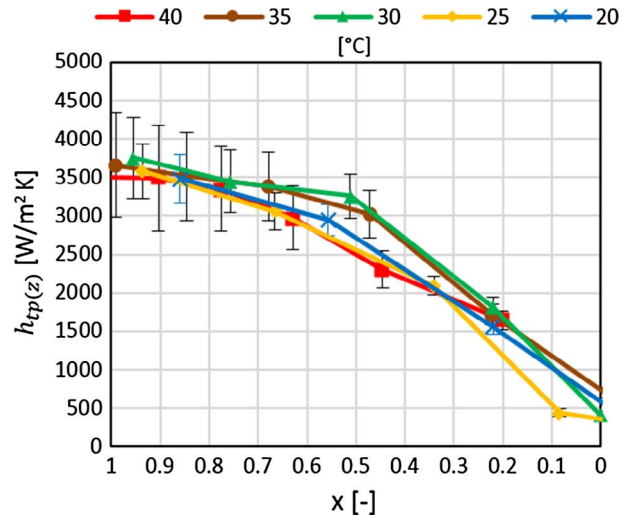


Fig. 18. Effect of inlet coolant temperature on the local condensation heat transfer coefficient at mass flux of 86 kg/m² s and coolant flow rate of 0.5 L/min.

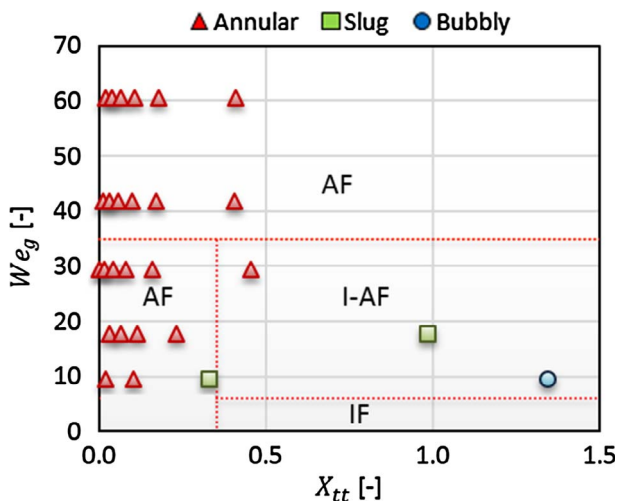


Fig. 16. Comparison of the present results with the map of Nema et al. [54] at a coolant flow rate of 0.5 L/min and inlet coolant temperature of 40 °C. (AF: Annular flow, I-AF: Intermittent-annular flow, IF: Intermittent flow).

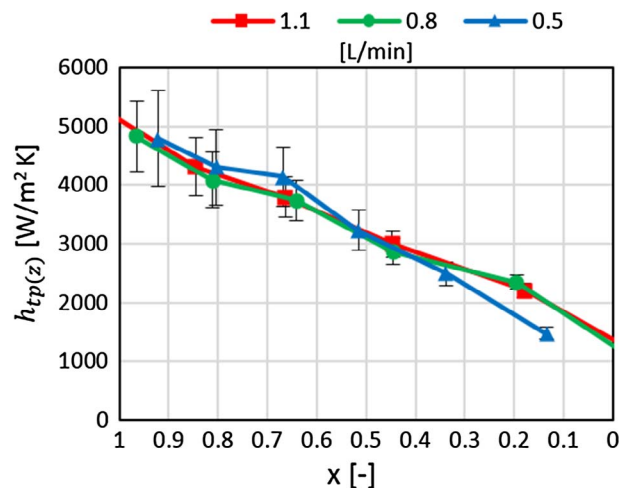


Fig. 19. Effect of coolant flow rate on the local condensation heat transfer coefficient at mass flux of 126 kg/m² s and inlet coolant temperature of 30 °C.

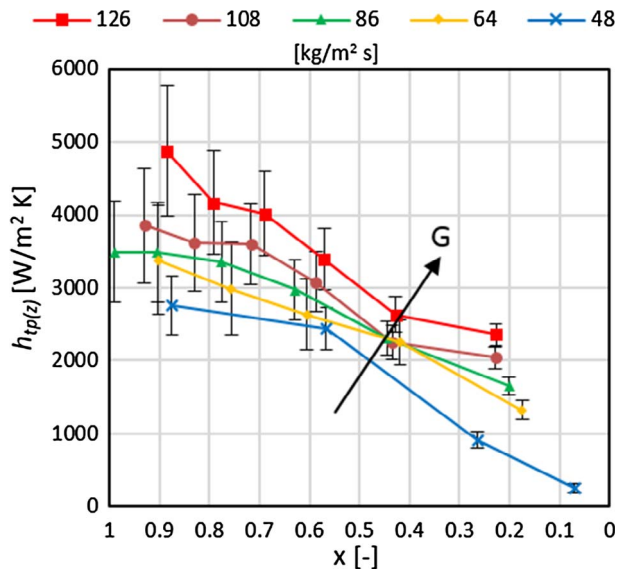


Fig. 20. Effect of mass flux on the local condensation heat transfer coefficient at coolant flow rate of 0.5 L/min and inlet coolant temperature of 40 °C.

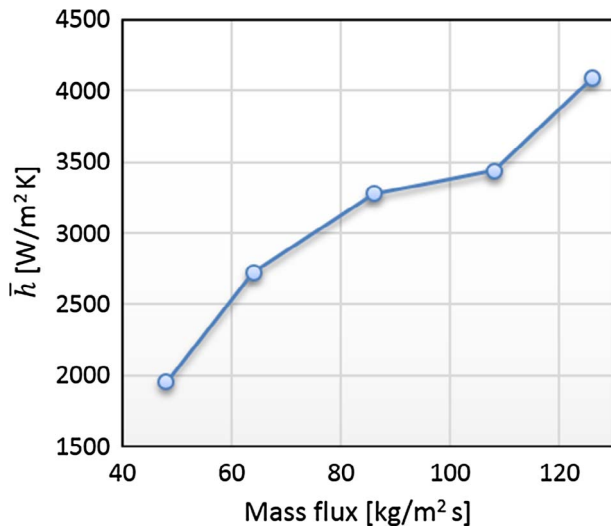


Fig. 21. Average heat transfer coefficient at different mass fluxes, coolant flow rate of 0.5 L/min and inlet coolant temperature of 40 °C.

4.3. Two-phase heat transfer

Flow condensation experiments were carried out at inlet vapour quality between 0.95 and 1 and saturation temperature of 60 °C. The effect of a number of parameters such as inlet coolant temperature, coolant flow rate, local vapour quality and refrigerant mass flux on the local condensation heat transfer coefficient was investigated. Fig. 17 shows the local heat transfer coefficient versus local vapour quality at mass flux of 108 kg/m² s, coolant flow rate of 1.1 L/min and inlet coolant temperature of 20 °C. It demonstrates that when the fluid enters the condenser, the flow pattern is annular and the local heat transfer coefficient is high. The local heat transfer coefficient decreases with decreasing local vapour quality due to the condensation process along the channels. This is due to the thickening of the liquid film leading to higher fluid thermal resistance.

In order to study the effect of saturation-to-wall temperature difference, the coolant side conditions were varied during the experiments, e.g. inlet coolant temperature and coolant flow rate. Five different inlet coolant temperatures of 20, 25, 30, 35 and 40 °C were used

as shown in Fig. 18. This figure depicts the local condensation heat transfer coefficient versus local vapour quality at mass flux of 86 kg/m² s and coolant flow rate of 0.5 L/min. It is obvious that there is no clear effect of the inlet coolant temperature on the local heat transfer coefficient.

Fig. 19 shows the effect of coolant flow rate on the local condensation heat transfer coefficient at mass flux of 126 kg/m² s and inlet coolant temperature of 30 °C. Three different coolant flow rates of 0.5, 0.8 and 1.1 L/min were tested. This figure demonstrates that, there is a negligible effect of coolant flow rate on the local heat transfer coefficient in the range studied. A variation of the coolant side, inlet coolant temperature or coolant flow rate, with keeping constant refrigerant side conditions results in a variation of the wall temperature and thus in the saturation-to-wall temperature difference. However, the temperature difference seems to have a negligible effect on the local condensation heat transfer coefficient in the range studied. Similar conclusion was found by other studies, such as Matkovic et al. [25,27] and Del Col et al. [29].

Five mass flux values of 48, 64, 86, 108 and 126 kg/m² s, coolant flow rate of 0.5 L/min and inlet coolant temperature of 40 °C were tested to study the effect of refrigerant mass flux on the condensation heat transfer coefficient. As seen in Figs. 20 and 21, the local and the average heat transfer coefficient increase with increasing mass flux. This was also found by Cavallini et al. [16], Agarwal et al. [17], Al-Hajri et al. [21] and Kim and Mudawar [6]. This increase was attributed by the previous authors to an increase in the shear stress between liquid and vapour phase leading to decreased liquid film thickness and thermal resistance of fluid. Therefore, the heat transfer coefficient increases with increasing mass flux. It can be concluded that, the interfacial shear stress is the dominating regime in this study. This is contrary to the results of Wang and Rose [14] since the surface tension was the dominant regime in their numerical study.

It is worth mentioning that, one of the main uses of the multi-microchannel condenser presented in this paper is the possibility that it can be used in a small scale liquid-pump cooling cycle for cooling electronic components. Therefore, the present condenser can achieve a cooling capacity of 520.2 W at a maximum mass flux of 126 kg/m² s and outlet sub-cooling temperature of 3.5 K. The operating conditions of coolant side are found at a lower coolant flow rate of 0.5 L/min, which means lower power consumption by the coolant pump, and standard coolant temperature of 30 °C. This capacity at the condenser corresponds to a heat flux of 1 MW/m² for a chip die size of 20 mm × 25 mm (500 mm²), i.e. possible cooling capacity at the evaporator of an integrated thermal management system.

4.4. Evaluation of existing heat transfer correlations

The experimental condensation heat transfer coefficient with total data points of 217 is compared with a number of existing correlations. These correlations are divided into two groups; conventional and mini/microchannel, based on the classification of Kandlikar and Grande [55]. Their classification, originally referring to boiling was adopted by some researchers in flow condensation studies, [27,39,45]. The authors classified the channels based on the hydraulic diameter as follows:

- Conventional Channels: $D_h > 3$ mm
- Minichannels: $0.2 \text{ mm} < D_h \leq 3$ mm
- Microchannels: $0.2 \text{ mm} \geq D_h > 0.01$ mm
- Nanochannels: $D_h \leq 0.01$ mm.

To evaluate the accuracy of each correlation, the mean absolute error (MAE) and the percentage of data points predicted within $\pm 30\%$ error bands (Θ) are used as follows.

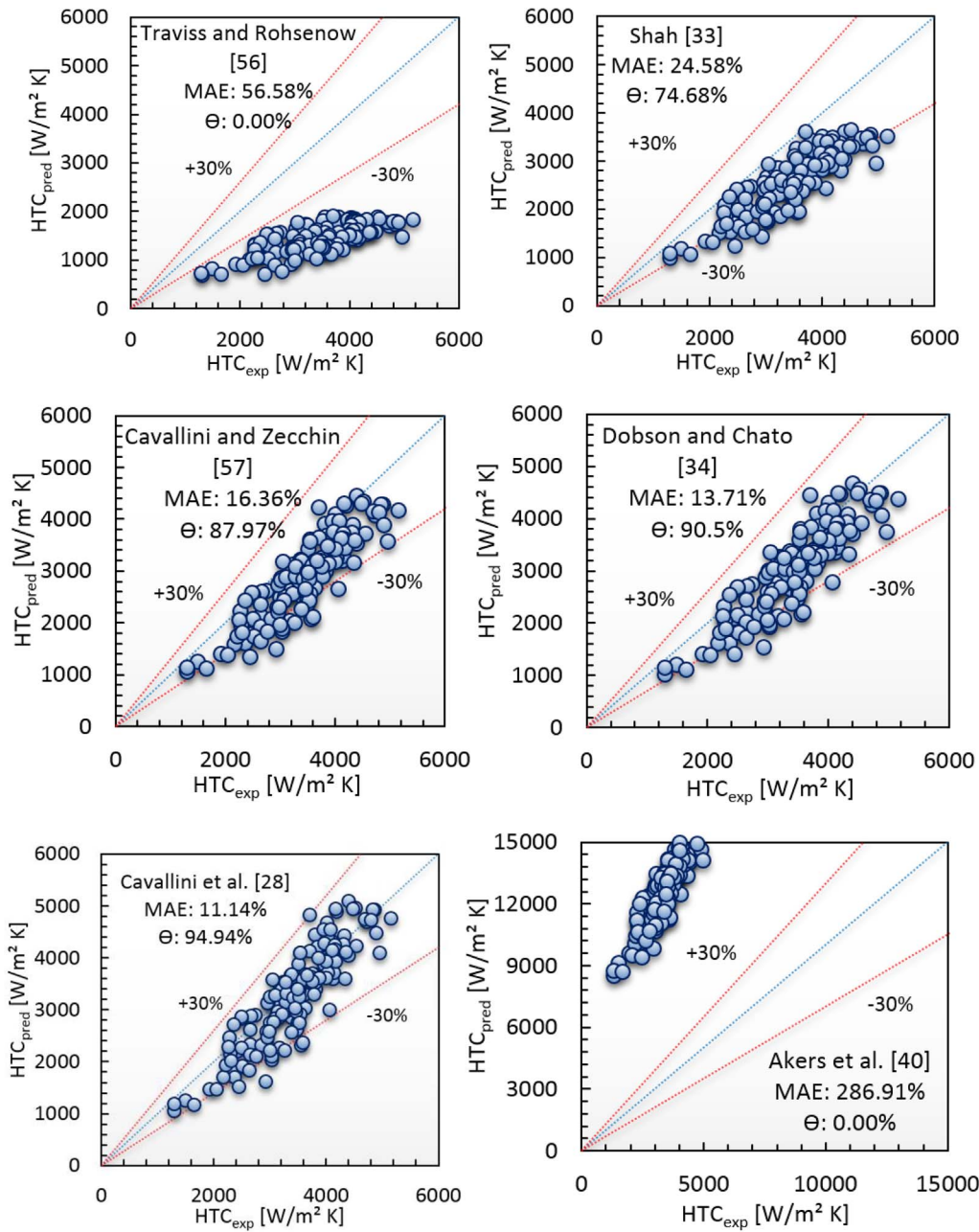


Fig. 22. Comparison between experimental data and the prediction correlations for annular condensation heat transfer coefficient in conventional channel.

$$MAE = \frac{1}{N} \sum \left| \frac{h_{pred} - h_{exp}}{h_{exp}} \right| * 100\% \quad (28)$$

$$\theta = \frac{N_{pred}}{N_{exp}} * 100\% \quad (29)$$

A summary of the existing correlations for the prediction of condensation heat transfer coefficients is presented in Appendix A. These correlations were proposed for circular tubes or rectangular channels with four-sides cooling. Therefore, a correction factor should be used to calculate the heat transfer coefficient with three-sides cooling as follows:

$$HTC = \left(\frac{Nu_3}{Nu_4} \right) * h_{tp} \quad (30)$$

where h_{tp}, Nu_3 and Nu_4 are the two phase heat transfer coefficient obtained from Appendix A, Nusselt number for thermally developed laminar flow with three-sides and four-sides heat transfer, respectively.

The above technique was adopted by Kim and Mudawar [6,44]. The following equations are used to find Nu_3 and Nu_4 , as proposed by Shah and London [49].

$$Nu_3 = 8.235(1 - 1.833\beta + 3.767\beta^2 - 5.814\beta^3 + 5.361\beta^4 - 2\beta^5) \quad (31)$$

$$Nu_4 = 8.235(1 - 2.042\beta + 3.085\beta^2 - 2.477\beta^3 + 1.058\beta^4 - 0.186\beta^5) \quad (32)$$

All correlations in Appendix A are for annular flow, except one of the two correlations of [44] which is for slug and bubbly flow. Therefore, the experimental data points are separated then compared as follows: 158 data points for annular flow and 59 data points, for slug and bubbly flow.

The comparison with the correlations proposed for conventional channels is shown in Fig. 22, including the correlations of Akers et al. [40], Traviss and Rohsenow [56], Cavallini and Zecchin [57], Shah [33], Dobson and Chato [34] and Cavallini et al. [28]. It seems that the correlation of Akers et al. [40] highly over predicts the experimental database with a mean absolute error of 286.91%. Also, the correlation

of Traviss and Rohsenow [56] highly under predicts the experimental database with a MAE of 56.58%. The correlation of Shah [33] and Cavallini and Zecchin [57] show a good prediction with a MAE of 24.58% and 16.36%, respectively. The best prediction was found when using the correlations by Dobson and Chato [34] and Cavallini et al. [28]. The first correlation can predict 90.5% of the data points with a MAE of 13.71%, while the second one predicts 94.94% of data with a MAE of 11.14%. It is worth mentioning that, the correlation of Cavallini et al. [28] also showed very good agreement with the experimental results by Matkovic et al. [27], although their experiments were conducted in a circular channel with inner diameter of 0.96 mm.

Fig. 23 shows the comparison with the mini/microchannels correlations. Wang and Rose [14] proposed a theoretical model for condensation in microchannels. This model does not show a good prediction with a MAE of 335.15%. This could be due to the fact that this model was developed for surface tension dominated regime, which is not the case here. The correlation of Wang et al. [58] and Bohdal et al. [39] highly over predict the experimental data with a MAE of 120.19% and 65.78%, respectively. The correlation of Koyama et al. [35] is able to predict 34.81% of the total points with a MAE of 36.87%. The correlation of Park et al. [41] predicts 71.52% of the total 113 data points, with a MAE of 23.97%. The correlation of Shah [45] predicts the experimental database well with a MAE of 16.39% and Θ of 91.77%. The

best comparison was with the correlation for mini/microchannels proposed by Kim and Mudawar [44]. This correlation is able to predict 143 points with a MAE of 14.95% and Θ of 90.51%. The authors also proposed another correlation for slug and bubbly flow. Therefore, this correlation was used to compare with 59 data points for these regimes, see Fig. 23 which demonstrates significant scatter for the 33 points used in the comparison.

These correlations were able to predict the experimental results with reasonable accuracy: Dobson and Chato [34] and Cavallini et al. [28] correlations proposed for conventional channels and Kim and Mudawar [44] and Shah [45] correlations for mini/microchannel with a mean absolute error of 13.71%, 11.14%, 14.95% and 16.39%, respectively. It can also be concluded that a correlation for conventional channel may be used for multi-microchannels, at least for the size used in the present study, as shown by the correlation of Dobson and Chato [34] and Cavallini et al. [28] in the range studied. However, more studies are required to confirm this point for different operating conditions, fluids and channel geometries.

5. Conclusions

Flow condensation of HFE-7100 in horizontal multi-microchannels with a hydraulic diameter of 0.57 mm was performed. All experiments were

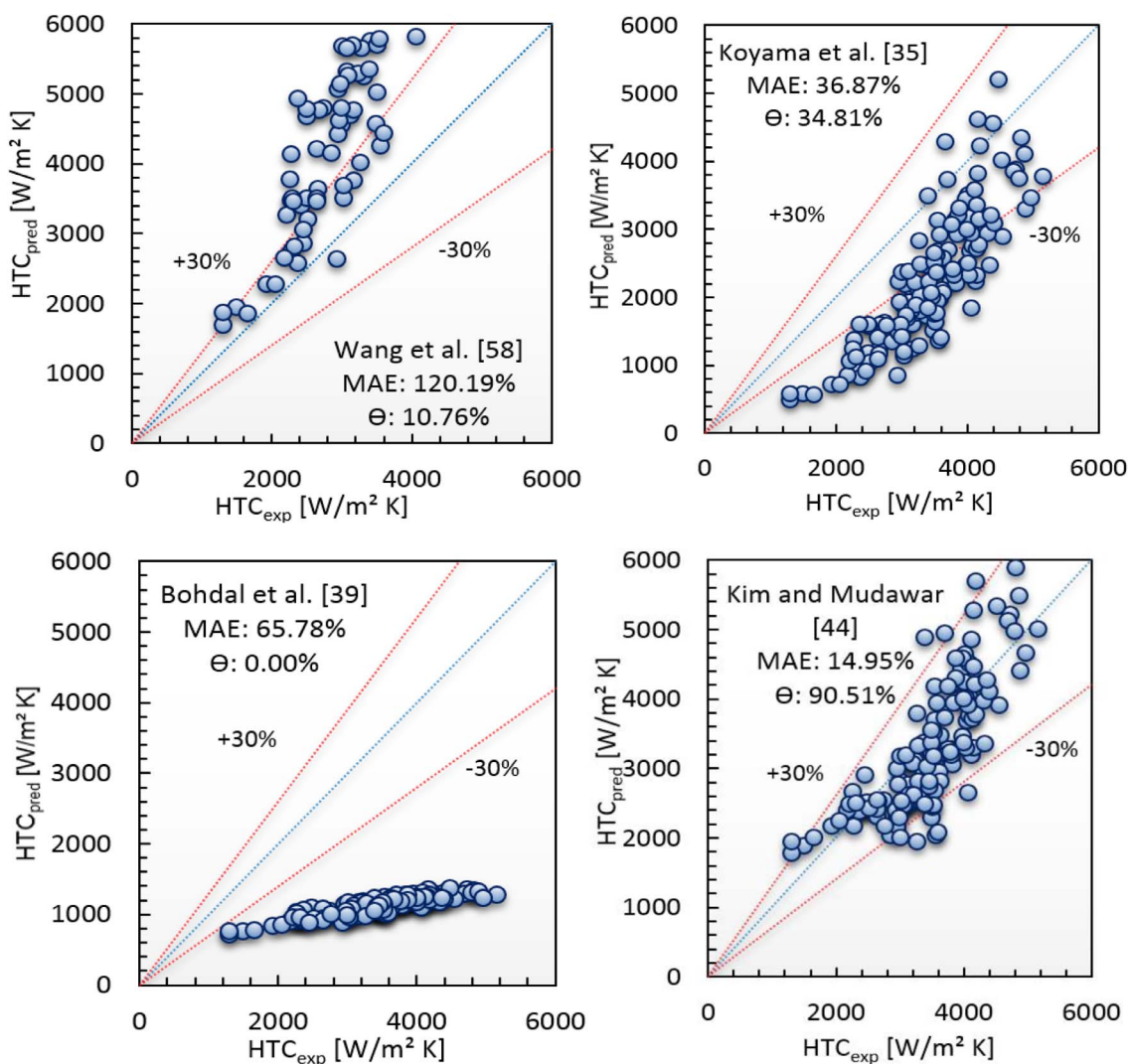


Fig. 23. Comparison between experimental data and the prediction correlations for annular condensation heat transfer coefficient in mini/microchannel, and the correlation of Kim and Mudawar [44] for slug/bubbly flow.

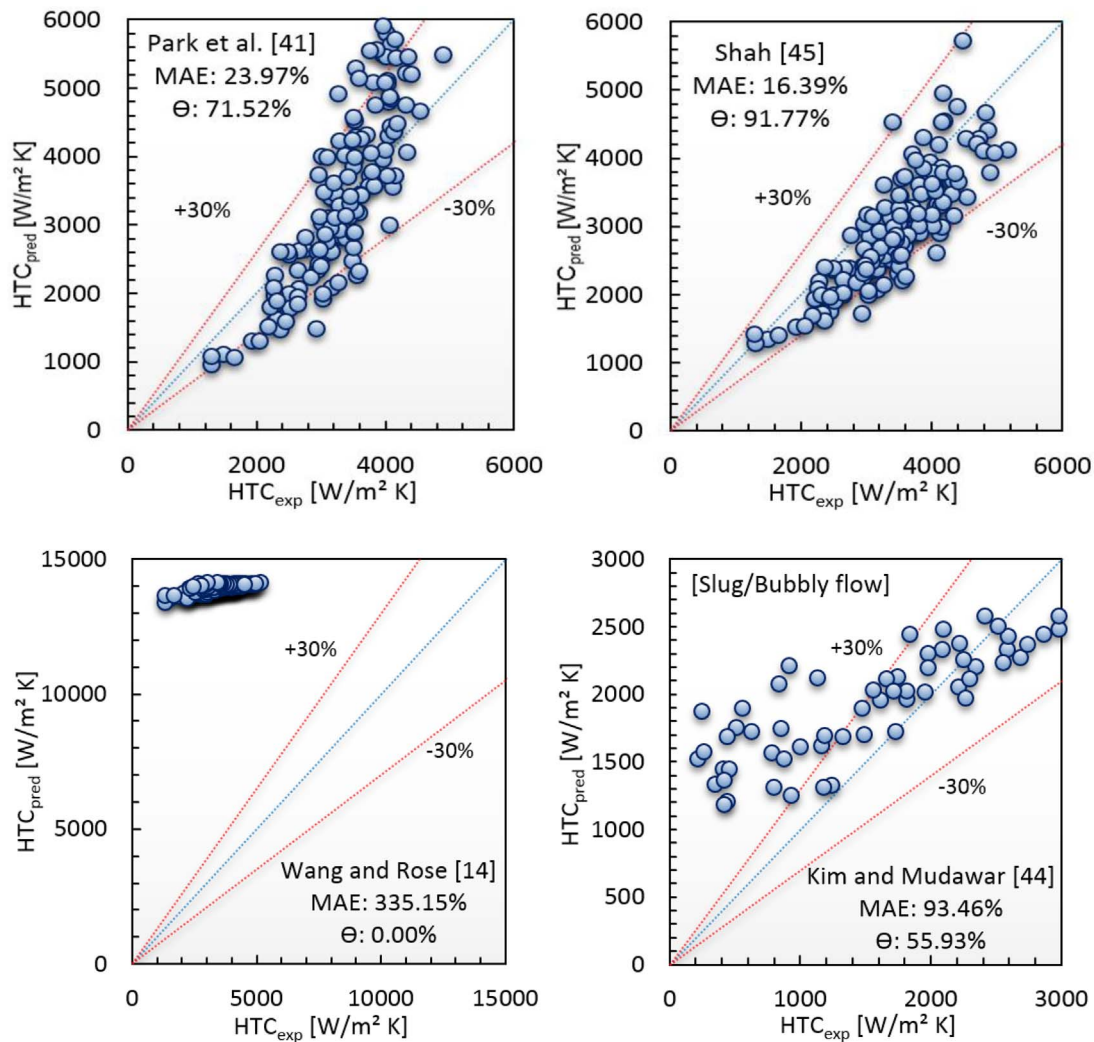


Fig. 23. (continued)

conducted at saturation temperature of 60 °C, mass flux ranging from 48 to 126 kg/m² s, coolant flow rate from 0.5 to 1.1 L/min and inlet coolant temperature from 20 to 40 °C. The effect of refrigerant mass flux, local vapour quality, coolant flow rate and inlet coolant temperature on the local condensation heat transfer coefficient were studied. A high-speed camera was used to capture the flow patterns during the flow condensation. Main points can be summarized as follows:

- Single phase validation results showed a good agreement between experimental fanning friction factor and the correlation of Shah and London [49] for fully developed laminar flow. The trend of the Nusselt number versus Reynolds number was similar to that of Peng and Peterson [51] and Bejan [52].
- Local condensation heat transfer coefficient increases with increasing refrigerant mass flux. Also, it decreases with decreasing local vapour quality.
- Saturation-to-wall temperature difference seems to have a negligible effect on the local condensation heat transfer coefficient.
- At higher mass fluxes, annular flow is the prevalent regime, while at lower mass fluxes, slug and bubbly flow are also found.
- It can be concluded that the interfacial shear stress is the dominant regime at this scale and with this particular fluid.
- When the condensation rate increases, decreasing inlet coolant temperature or increasing coolant flow rate, annular, slug and

bubbly regimes shift to the right on the G versus x flow map, i.e. higher vapour quality.

- The flow patterns maps of Cavallini et al. [53] and Nema et al. [54] are able to predict the annular flow regime but not the other flow patterns.
- Fourteen existing correlations of the condensation heat transfer coefficient in conventional and mini/microchannels were compared with the experimental results. This comparison showed that only the correlations of Dobson and Chato [34], Cavallini et al. [28], Kim and Mudawar [44] and Shah [45] are able to predict the results within acceptable limits, i.e. with a mean absolute error of 13.71%, 11.14%, 14.95% and 16.39%, respectively.
- The correlation of Dobson and Chato [34] and Cavallini et al. [28] for conventional channel could probably be used to obtain the annular condensation heat transfer coefficient in multi-microchannels down to the hydraulic diameter of 0.57 mm of this study. However, more studies are required to confirm this, using different operating conditions, fluids and channel geometries.
- The present multi-microchannel condenser could achieve a cooling capacity of 520.2 W at a low coolant flow rate and standard coolant temperature. This corresponds to the heat flux of 1 MW/m² for a chip die size of 20 mm × 25 mm (500 mm²) when such a condenser forms part of a small-scale thermal management system for high heat flux devices.

Acknowledgements

Ali Al-Zaidi would like to thank the Iraqi Ministry of Higher

Education and Scientific Research (MOHESR) for their financial support for his PhD programme at Brunel University London. The financial support of EPSRC under grant EP/K011502/1 is also acknowledged.

Appendix A. Condensation heat transfer correlations

Author(s)	Correlation	Remarks
Akers et al. [40]	$h_{ip} = 5.03 * Re_{eq}^{1/3} * Pr_l^{1/3} * k_f / D_h$ $Re_{eq} = G * \left[(1-x) + x * \left(\frac{\rho_l}{\rho_g} \right)^{0.5} \right] * D_h / \mu_l$	Fluids (propane, R12) $Re_{eq} \leq 50,000$
Traviss and Rohsenow [56]	$h_{ip} = \left[\frac{0.15 * Re_{ls}^{0.9} * Pr_l}{F} \right] * \left[\frac{1}{X_{tt}} + \frac{2.89}{X_{tt}^{0.478}} \right] * k_f / D$ $F = 5Pr_l + 5 \ln(1 + 5Pr_l) + \ln(0.09636 * Re_{ls}^{0.812} - 1) \text{ For } Re_{ls} > 50$ $F = 0.707 * Pr_l * Re_{ls}^{0.5} \text{ For } Re_{ls} < 50$	Fluid (R22) $D = 8 \text{ mm}$
Cavallini and Zecchin [57]	$h_{ip} = 0.05 * Re_{ls}^{0.8} * Pr_l^{0.33} * \left[1 + \left(\frac{\rho_l}{\rho_g} \right)^{0.5} * \left(\frac{x}{1-x} \right) \right]^{0.8} * k_f / D$	Fluids (R12, R22, R113)
Shah [33]	$h_{ip} = 0.023 * Re^{0.8} * Pr_l^{0.4} * \left[(1-x)^{0.8} + \frac{3.8 * x^{0.76} * (1-x)^{0.04}}{Pr_R^{0.38}} \right] * k_f / D_h$	Fluids (Benzene, Ethanol, Toluene, Water, Methanol, Trichloroethyle, R11, R12, R22, R113,) $D = 7-40 \text{ mm}$
Dobson and Chato [34]	$h_{ip} = 0.023 * Re_{ls}^{0.8} * Pr_l^{0.4} * \left[1 + \frac{2.22}{X_{tt}^{0.89}} \right] * k_f / D_h$	Fluids (R134a, R12, R22, R32/R125) $D = 3.14-7.04 \text{ mm}$
Wang et al. [58]	$h_{ip} = 0.0274 * Re_{ls}^{0.6792} * Pr_l * x^{0.2208} * \left[\frac{\phi_g}{X_{tt}} \right] * k_f / D_h$ $\phi_g = [1.376 + 8 * X_{tt}^{1.665}]^{0.5}$	Fluid (R134a) $D_h = 1.46 \text{ mm}$ Multi-channel
Koyama et al. [35]	$h_{ip} = 0.0152 * Re_{ls}^{0.77} * (1 + 0.6 * Pr_l^{0.8}) * \left[\frac{\phi_g}{X_{tt}} \right] * k_f / D_h$ $\phi_g = [1 + 21(1 - \exp(-0.319 * D_h)) * X_{tt} + X_{tt}^2]^{0.5}$	Fluid (R134a) $D_h = 0.8-.11 \text{ mm}$ Multi-channel
Cavallini et al. [28]	<p>For annular flow, ΔT-independent flow regime ($J_G > J_G^T$):</p> $h_{ip,1} = h_{sp} \left[1 + 1.128x^{0.817} \left(\frac{\rho_l}{\rho_g} \right)^{0.3685} \left(\frac{\mu_l}{\mu_g} \right)^{0.2363} * (1 - \mu_g / \mu_l)^{2.144} * Pr_l^{-0.1} \right]$ <p>For stratified-wavy or smooth flow, ΔT-dependent flow regime ($J_G \leq J_G^T$):</p> $h_{ip,2} = [h_{ip,1} \left(\frac{J_G^T}{J_G} \right)^{0.8} - h_{ip,3}] \left(\frac{J_G}{J_G^T} \right) + h_{ip,3}$ <p>For slug flow, both $h_{ip,1}$ and $h_{ip,2}$</p> $h_{ip,3} = 0.725 \left(1 + 0.741 \left[\frac{(1-x)}{x} \right]^{0.3321} \right)^{-1} * \left[\frac{k_f^3 * \rho_l * \Delta \rho * g * i_g}{\mu_l * D * \Delta T} \right]^{0.25} + (1-x)^{0.087} * h_{sp}$ $h_{sp} = 0.023 * Re^{0.8} * Pr_l^{0.4} * k_f / D$ $J_G^T = ([7.5 / (4.3 * X_{tt}^{1.111} + 1)]^{-3} + C_T^{-3})^{-0.333}$ $C_T = 1.6 \text{ (for hydrocarbons)}$ $C_T = 2.6 \text{ (for other refrigerants)}$ $\Delta T = T_{sat} - T_{wi}$	Fluid (R134a, R125, R236ea, R32, R410A) $D > 3 \text{ mm}$
Wang and Rose [14]	$h_{ip} = 1.43 * \left[\frac{\rho_l * i_g * \sigma * b}{\mu_l * k_f * \Delta T} \right]^{0.25} * k_f / D_h$ $\Delta T = T_{sat} - T_{wi}$ $b = (2H_{ch} + W_{ch}) / 3$	Fluids (R134, R152a, R22, R410A, Ammonia, Carbon dioxide, Propane) Different geometries
Bohdal et al. [39]	$h_{ip} = 25.084 * Re_{ls}^{0.258} * Pr_l^{-0.495} * Pr_R^{-0.288} * \left[\frac{x}{1-x} \right]^{0.266} * k_f / D$	Fluids (R134a, R404A) $D = 0.31-3.3 \text{ mm}$
Park et al. [41]	$h_{ip} = 0.0055 * Re_{ls}^{0.7} * Pr_l^{1.37} * \left[\frac{\phi_g}{X_{tt}} \right] * k_f / D_h$ $\phi_g = \left[1 + 13.17 \left(\frac{\rho_g}{\rho_l} \right)^{0.17} * \left(1 - \exp \left(-0.6 \sqrt{\frac{g * \Delta \rho * D_h^2}{\sigma}} \right) \right) \right] * X_{tt} + X_{tt}^2 \right]^{0.5}$	Fluids (R134a, R1234ze(E), R236fa) $D_h = 1.45 \text{ mm}$ Multi-channel
Kim and Mudawar [44]	<p>For annular flow where $We^* > 7X_{tt}^{0.2}$</p> $h_{ip} = 0.048 * Re_{ls}^{0.69} * Pr_l^{0.34} * \left[\frac{\phi_g}{X_{tt}} \right] * k_f / D_h$ <p>For slug and bubbly flow where $We^* < 7X_{tt}^{0.2}$</p> $h_{ip} = \left[(0.048 * Re_{ls}^{0.69} * Pr_l^{0.34} * \left[\frac{\phi_g}{X_{tt}} \right])^2 + (3.2 * 10^{-7} * Re_{ls}^{-0.38} * Su_{go}^{1.39})^2 \right]^{0.5} * k_f / D_h$ $\phi_g^2 = 1 + CX + X^2$	17 different fluids $D_h = 0.42-6.2 \text{ mm}$ Single/multi-channel

$$X = \sqrt{\frac{(dP/dz)_l}{(dP/dz)_g}}$$

$$\left(\frac{dP}{dz}\right)_l = \frac{2 * f_l * v_l * G^2 * (1-x)^2}{D_h}$$

$$\left(\frac{dP}{dz}\right)_g = \frac{2 * f_g * v_g * G^2 * x^2}{D_h}$$

For turbulent- turbulent ($Re_{ls} \geq 2000, Re_{gs} \geq 2000$): $C = 0.39Re^{0.03} Su_{go}^{0.1} \left(\frac{\rho_l}{\rho_g}\right)^{0.35}$

Turbulent- laminar

($Re_{ls} \geq 2000, Re_{gs} < 2000$): $C = 8.7 \times 10^{-4} Re^{0.17} Su_{go}^{0.5} \left(\frac{\rho_l}{\rho_g}\right)^{0.14}$

Laminar- turbulent ($Re_{ls} < 2000, Re_{gs} \geq 2000$): $C = 0.001Re^{0.59} Su_{go}^{0.19} \left(\frac{\rho_l}{\rho_g}\right)^{0.36}$

Laminar- laminar ($Re_{ls} < 2000, Re_{gs} < 2000$): $C = 3.5 \times 10^{-5} Re^{0.44} Su_{go}^{0.5} \left(\frac{\rho_l}{\rho_g}\right)^{0.48}$

$We^* = 2.45 \frac{Re_{gs}^{0.64}}{Su_{go}^{0.3} (1 + 1.09X_l^{0.039})^{0.4}}$ For $Re_{ls} \leq 1250$

$We^* = 0.85 \frac{Re_{gs}^{0.79} * X_l^{0.157}}{Su_{go}^{0.3} (1 + 1.09X_l^{0.039})^{0.4}} \left[\left(\frac{\mu_g}{\mu_l}\right)^2 * \left(\frac{v_g}{v_l}\right) \right]^{0.084}$ For $Re_{ls} > 1250$

$f_k Re_{ks} = 24(1 - 1.355\beta + 1.946\beta^2 - 1.7012\beta^3 + 0.9564\beta^4 - 0.2537\beta^5)$
($k = l$ or g) for laminar flow in a rectangular channel ($\beta < 1$)

Shah [45]

$h_{tp} = h_l$ For region I

$h_{tp} = h_l + h_{NU}$ For region II

$h_l = h_{NU}$ For region III

$h_l = h_{LT} \left[1 + 1.128x^{0.817} \left(\frac{\rho_l}{\rho_g}\right)^{0.3685} * \left(\frac{\mu_l}{\mu_g}\right)^{0.2363} * \left(1 - \frac{\mu_g}{\mu_l}\right)^{2.144} * Pr_l^{-0.1} \right]$

$h_{NU} = 1.32 * Re_{ls}^{-1/3} \left[\frac{\rho_l(\rho_l - \rho_g)g * k_f^3}{\mu_l^2} \right]^{1/3}$

$h_{LT} = 0.023 * Re^{0.8} * Pr_l^{0.4} * k_f / D_h$

For region I: $J_G \geq 0.98(Z + 0.263)^{-0.62}$ and $We_g \geq 100$

For region III: $J_G \leq 0.95(1.254 + 2.27 * Z^{1.249})^{-1}$

For region II: if the above criteria do not match

$D_h = \frac{4 * \text{cross section area}}{\text{perimeter}}$ 'For Weber number'

$D_h = \frac{4 * \text{cross section area}}{\text{perimeter with heat transfer}}$ 'For all equations'

13 different fluids $D_h = 0.1-2.8$ mm Various shapes Single/multi-channel

Appendix B. Single phase correlations

Author(s)	Correlation	Remarks
Shah and London [49]	$f = (24(1 - 1.355\beta + 1.946\beta^2 - 1.7012\beta^3 + 0.9564\beta^4 - 0.2537\beta^5)) / Re$	For laminar fully developed flow, non-circular ducts
Peng and Peterson [51]	$Nu = 0.1165 \left[\frac{D_h}{W_c} \right]^{0.81} * \left[\frac{H_{ch}}{W_{ch}} \right]^{-0.79} * Re^{0.62} * Pr^{1/3}$ $W_c = W_{ch} + W_{fin}$	For laminar flow, rectangular microchannels
Bejan [52]	$Nu = 1.5(L/Re * D_h * Pr)^{-0.5}$	For laminar flow, non-circular ducts

References

- [1] W. Qu, I. Mudawar, Flow boiling heat transfer in two-phase micro-channel heat sinks-I. Experimental investigation and assessment of correlation methods, Int. J. Heat Mass Transf. (2003) 2755–2771.
- [2] K. Balasubramanian, M. Jagirdar, P.S. Lee, C.J. Teo, S.K. Chou, Experimental investigation of flow boiling heat transfer and instabilities in straight microchannels, Int. J. Heat Mass Transf. 66 (2013) 655–671.
- [3] B. Markal, O. Aydin, M. Avci, Effect of aspect ratio on saturated flow boiling in microchannels, Int. J. Heat Mass Transf. 93 (2016) 130–143.
- [4] D. Del Col, S. Bortolin, E. Da Riva, Encyclopedia of two-phase heat transfer and flow: Special topics and applications Prediction Methods and Numerical Modeling of Condensation Heat Transfer in Minichannels, chapter three, World Scientific Publishing Co., Singapore, 2016.
- [5] D. Del Col, M. Bortolato, M. Azzolin, S. Bortolin, Effect of inclination during condensation inside a square cross section minichannel, Int. J. Heat Mass Transf. 78 (2014) 760–777.
- [6] S. Kim, I. Mudawar, Flow condensation in parallel micro-channels – Part 2: Heat transfer results and correlation technique, Int. J. Heat Mass Transf. 55 (4) (2012) 984–994.
- [7] J. Zhang, W. Li, Numerical study on heat transfer and pressure drop characteristics of R410A condensation in horizontal circular mini/micro tubes, Can. J. Chem. Eng. 94 (9) (2016) 1809–1819.
- [8] X. Ma, X. Fan, Z. Lan, T. Hao, Flow patterns and transition characteristics for steam condensation in silicon microchannels, J. Micromech. Microeng. 21 (2011) 075009.
- [9] Y. Chen, J. Wu, R. Wu, M. Shi, G.P. Peterson, Visualization study of steam condensation in triangular microchannels, Int. J. Heat Mass Transf. 52 (21) (2009) 5122–5129.
- [10] S. Kim, J. Kim, I. Mudawar, Flow condensation in parallel micro-channels – Part1: Experimental results and assessment of pressure drop correlations, Int. J. Heat Mass Transf. 55 (4) (2012) 971–983.
- [11] R. Jiang, X. Ma, Z. Lan, Y. Bai, T. Bai, Visualization study of condensation of ethanol–water mixtures in trapezoidal microchannels, Int. J. Heat Mass Transf. 90 (2015) 339–349.
- [12] S. Chen, Z. Yang, Y. Duan, Y. Chen, D. Wu, Simulation of condensation flow in a rectangular microchannel, Chem. Eng. Process. 76 (2014) 60–69.
- [13] G. El Achkar, M. Miscevic, P. Lavieille, Experimental study of slug flow for

- condensation in a square cross section micro-channel at low mass velocities', 4th Micro and Nano Flows Conference (MNF2014), Brunel University London, 2014.
- [14] H.S. Wang, J.W. Rose, Theory of heat transfer during condensation in micro-channels, *Int. J. Heat Mass Transf.* 54 (11) (2011) 2525–2534.
- [15] E. Da Riva, D. Del Col, Numerical simulation of laminar liquid film condensation in a horizontal circular minichannel, *J. Heat Transf.* 134 (5) (2012) 051019.
- [16] A. Cavallini, D. Del Col, L. Doretti, M. Matkovic, L. Rossetto, C. Zilio, Condensation heat transfer and pressure gradient inside multiport minichannels, *Heat Transf. Eng.* 26 (3) (2005) 45–55.
- [17] A. Agarwal, T.M. Bandhauer, S. Garimella, Measurement and modeling of condensation heat transfer in non-circular microchannels, *Int. J. Refrig.* 33 (6) (2010) 1169–1179.
- [18] B.M. Fronk, S. Garimella, Heat transfer and pressure drop during condensation of ammonia in microchannels, in: *ASME 3rd Micro/Nanoscale Heat and Mass Transfer International Conference*, March 3–6, Atlanta, GA, 2012.
- [19] D. Del Col, M. Bortolato, M. Azzolin, S. Bortolin, Condensation heat transfer and two-phase frictional pressure drop in a single minichannel with R1234ze(E) and other refrigerants, *Int. J. Refrig.* 50 (2015) 87–103.
- [20] D. Jige, N. Inoue, S. Koyama, Condensation of refrigerants in a multiport tube with rectangular minichannels, *Int. J. Refrig.* 67 (2016) 202–213.
- [21] E. Al-Hajri, A.H. Shoostari, S. Dessiatoun, M.M. Ohadi, Performance characterization of R134a and R245fa in a high aspect ratio microchannel condenser, *Int. J. Refrig.* 36 (2) (2013) 588–600.
- [22] J. Heo, H. Park, R. Yun, Condensation heat transfer and pressure drop characteristics of CO₂ in a microchannel, *Int. J. Refrig.-Revue Int. Du Froid* 36 (6) (2013) 1657–1668.
- [23] F. Illan-Gomez, A. Lopez-Belchi, J. Garcia-Cascales, F. Vera-Garcia, Experimental two-phase heat transfer coefficient and frictional pressure drop inside mini channels during condensation with R1234yf and R134a, *Int. J. Refrig.-Revue Int. Du Froid* 51 (2015) 12–23.
- [24] N. Liu, J.M. Li, J. Sun, H.S. Wang, Heat transfer and pressure drop during condensation of R152a in circular and square microchannels, *Exp. Therm. Fluid Sci.* 47 (2013) 60–67.
- [25] M. Matkovic, S. Bortolin, A. Cavallini, D. Del Col, Experimental study of condensation inside a horizontal single square minichannel, in: *ASME 2nd Micro/Nanoscale Heat and Mass Transfer International Conference*, December 18–21, Shanghai, China, 2009, pp. 147–154.
- [26] S. Bortolin, E. Da Riva, D. Del Col, Condensation in a square minichannel: application of the VOF method', *Heat Transf. Eng.* 35 (2) (2014) 193–203.
- [27] M. Matkovic, A. Cavallini, D. Del Col, L. Rossetto, Experimental study on condensation heat transfer inside a single circular minichannel, *Int. J. Heat Mass Transf.* 52 (9) (2009) 2311–2323.
- [28] A. Cavallini, D. Del Col, L. Doretti, M. Matkovic, L. Rossetto, C. Zilio, G. Censi, Condensation in horizontal smooth tubes: a new heat transfer model for heat exchanger design, *Heat Transf. Eng.* 27 (8) (2006) 31–38.
- [29] D. Del Col, S. Bortolin, A. Cavallini, M. Matkovic, Effect of cross sectional shape during condensation in a single square minichannel, *Int. J. Heat Mass Transf.* 54 (17) (2011) 3909–3920.
- [30] E. Da Riva, D. Del Col, S.V. Garimella, A. Cavallini, The importance of turbulence during condensation in a horizontal circular minichannel, *Int. J. Heat Mass Transf.* 55 (13) (2012) 3470–3481.
- [31] K. Sakamatapan, S. Wongwises, Pressure drop during condensation of R134a flowing inside a multiport minichannel, *Int. J. Heat Mass Transf.* 75 (2014) 31–39.
- [32] G. Goss, J.L.G. Oliveira, J.C. Passos, Pressure drop during condensation of R 134a inside parallel microchannels, *Int. J. Refrig.* 56 (2015) 114–125.
- [33] M.M. Shah, A general correlation for heat transfer during film condensation inside pipes, *Int. J. Heat Mass Transf.* 22 (4) (1979) 547–556.
- [34] M.K. Dobson, J.C. Chato, Condensation in smooth horizontal tubes, *J. Heat Transf.* 120 (1) (1998) 193–213.
- [35] S. Koyama, K. Kuwahara, K. Nakashita, K. Yamamoto, An experimental study on condensation of refrigerant R134a in a multi-port extruded tube, *Int. J. Refrig.* 26 (4) (2003) 425–432.
- [36] K.W. Moser, R.L. Webb, B. Na, A new equivalent Reynolds number model for condensation in smooth tubes, *ASME J. Heat Transf.* 120 (1998) 410–417.
- [37] H. Haraguchi, S. Koyama, T. Fujii, Condensation of refrigerants HCFC22, HFC134a and HCFC123 in a horizontal smooth tube (2nd report, proposal of empirical expressions for the local heat transfer coefficient), *Trans. JSME (B)* 60 (574) (1994) 245–252.
- [38] K. Mishima, T. Hibiki, Effect of inner diameter on some characteristics of air-water two-phase flows in capillary tubes, *Trans. JSME (B)* 61 (589) (1995) 99–106.
- [39] T. Bohdal, H. Charun, M. Sikora, Comparative investigations of the condensation of R134a and R404A refrigerants in pipe minichannels, *Int. J. Heat Mass Transf.* 54 (2011) 1963–1974.
- [40] W.W. Akers, H.A. Deans, O.K. Crosser, Condensing heat transfer within horizontal tubes, *Chem. Eng. Prog.* 54 (1958) 89–90.
- [41] J.E. Park, F. Vakili-Farahani, L. Consolini, J.R. Thome, Experimental study on condensation heat transfer in vertical minichannels for new refrigerant R1234ze(E) versus R134a and R236fa, *Exp. Therm. Fluid Sci.* 35 (3) (2011) 442–454.
- [42] S. Koyama, K. Kuwahara, K. Nakashita, Condensation of refrigerant in a multi-port channel, in: *International Conference on Microchannels and Minichannels*, New York, 2003, pp. 193–205.
- [43] A. Cavallini, L. Doretti, M. Matkovic, L. Rossetto, Update on condensation heat transfer and pressure drop inside minichannels, *Heat Transf. Eng.* 27 (4) (2006) 74–87.
- [44] S. Kim, I. Mudawar, Universal approach to predicting heat transfer coefficient for condensing mini/micro-channel flow, *Int. J. Heat Mass Transf.* 56 (2) (2013) 238–250.
- [45] M.M. Shah, A correlation for heat transfer during condensation in horizontal mini/micro channels, *Int. J. Refrig.* 64 (2016) 187–202.
- [46] M.M. Shah, General correlation for heat transfer during condensation in plain tubes: further development and verification, *ASHRAE Trans.* 119 (2) (2013) 3–11.
- [47] R. Remsburg, *Thermal design of electronic equipment*, Boca Raton, CRC Press, Fla., 2001.
- [48] R.J. Phillips, *Forced convection, liquid cooled, microchannel heat sinks*, MS Thesis Department of Mechanical Engineering, Massachusetts Institute of Technology, Cambridge, 1988.
- [49] R.K. Shah, A.L. London, *Laminar flow forced convection in ducts, a source book for compact heat exchanger analytical data*, Supl 1, Academic Press, New York, 1978.
- [50] H.W. Coleman, W.G. Steele, *Experimentation and uncertainty analysis for engineers*, third ed., Wiley, Chichester, New York, 2009.
- [51] X.F. Peng, G.P. Peterson, Convective heat transfer and flow friction for water flow in microchannel structures, *Int. J. Heat Mass Transf.* 39 (12) (1996) 2599–2608.
- [52] A. Bejan, *Convection heat transfer*, third ed., Wiley, Hoboken, NJ, 2004.
- [53] A. Cavallini, G. Censi, D. Del Col, L. Doretti, G.A. Longo, L. Rossetto, Condensation of halogenated refrigerants inside smooth tubes, *HVAC & R Res.* 8 (4) (2002) 429–451.
- [54] G. Nema, S. Garimella, B. Fronk, Flow regime transitions during condensation in microchannels, *Int. J. Refrig.-Revue Int. Du Froid* 40 (2014) 227–240.
- [55] S. Kandlikar, W. Grande, Evolution of microchannel flow passages – thermo-hydraulic performance and fabrication technology, *Heat Transf. Eng.* 24 (1) (2003) 3–17.
- [56] D.P. Travis, W.M. Rohsenow, Flow regimes in horizontal two-phase flow with condensation', *ASHRAE Trans.* 79 (2) (1973) 31–39.
- [57] A. Cavallini, R. Zecchin, Dimensionless correlation for heat transfer in forced convection condensation, in: *Proc. Fifth Int. Heat Transfer Conf.*, Tokyo, Japan, vol. 3, 1974, pp. 309–313.
- [58] W.W. Wang, T.D. Radcliff, R.N. Christensen, A condensation heat transfer correlation for millimeter-scale tubing with flow regime transition, *Exp. Therm. Fluid Sci.* 26 (5) (2002) 473–485.